



**HAL**  
open science

## MUSEQuBES: characterizing the circumgalactic medium of redshift $\approx 3.3$ Ly $\alpha$ emitters

Sowgat Muzahid, Joop Schaye, Sebastiano Cantalupo, Raffaella Anna Marino, Nicolas Bouché, Sean Johnson, Michael Maseda, Martin Wendt, Lutz Wisotzki, Johannes Zabl

### ► To cite this version:

Sowgat Muzahid, Joop Schaye, Sebastiano Cantalupo, Raffaella Anna Marino, Nicolas Bouché, et al.. MUSEQuBES: characterizing the circumgalactic medium of redshift  $\approx 3.3$  Ly  $\alpha$  emitters. Monthly Notices of the Royal Astronomical Society, 2021, 508 (4), pp.5612-5637. 10.1093/mnras/stab2933 . hal-03431262

**HAL Id: hal-03431262**

**<https://hal.science/hal-03431262v1>**

Submitted on 3 May 2023

**HAL** is a multi-disciplinary open access archive for the deposit and dissemination of scientific research documents, whether they are published or not. The documents may come from teaching and research institutions in France or abroad, or from public or private research centers.

L'archive ouverte pluridisciplinaire **HAL**, est destinée au dépôt et à la diffusion de documents scientifiques de niveau recherche, publiés ou non, émanant des établissements d'enseignement et de recherche français ou étrangers, des laboratoires publics ou privés.

# MUSEQuBES: characterizing the circumgalactic medium of redshift $\approx 3.3$ Ly $\alpha$ emitters

Sowgat Muzahid<sup>1</sup>,<sup>1,2\*</sup> Joop Schaye<sup>3</sup>, Sebastiano Cantalupo<sup>4,5</sup>, Raffaella Anna Marino,<sup>5</sup> Nicolas F. Bouché<sup>6</sup>, Sean Johnson<sup>7</sup>, Michael Maseda<sup>3</sup>, Martin Wendt<sup>8</sup>, Lutz Wisotzki<sup>2</sup> and Johannes Zabl<sup>6,9</sup>

<sup>1</sup>IUCAA, Post Bag 04, Ganeshkhind, Pune 411007, India

<sup>2</sup>Leibniz-Institute for Astrophysics Potsdam (AIP), An der Sternwarte 16, D-14482 Potsdam, Germany

<sup>3</sup>Leiden Observatory, Leiden University, PO Box 9513, NL-2300 RA Leiden, the Netherlands

<sup>4</sup>Department of Physics, University of Milan Bicocca, Piazza della Scienza 3, I-20126 Milano, Italy

<sup>5</sup>Department of Physics, ETH Zürich, Wolfgang-Pauli-Strasse 27, CH-8093 Zürich, Switzerland

<sup>6</sup>Univ Lyon, Univ Lyon1, Ens de Lyon, CNRS, Centre de Recherche Astrophysique de Lyon UMR5574, F-69230 Saint-Genis-Laval, France

<sup>7</sup>Department of Astronomy, University of Michigan, 1085 S. University Ave, Ann Arbor, MI 48109, USA

<sup>8</sup>Institut für Physik und Astronomie, Universität Potsdam, Karl-Liebknecht-Str 24/25, D-14476 Golm, Germany

<sup>9</sup>Department of Astronomy & Physics, Saint Mary's University, 923 Robie Street, Halifax, Nova Scotia B3H 3C 3, Canada

Accepted 2021 October 6. Received 2021 October 4; in original form 2021 May 11

## ABSTRACT

We present the first characterization of the circumgalactic medium of Ly  $\alpha$  emitters (LAEs), using a sample of 96  $z \approx 3.3$  LAEs detected with the VLT/MUSE in fields centred on eight bright background quasars. The LAEs have low Ly  $\alpha$  luminosities ( $\sim 10^{42}$  erg s $^{-1}$ ) and star formation rates (SFRs)  $\sim 1 M_{\odot}$  yr $^{-1}$ , which for main-sequence galaxies correspond to stellar masses of only  $\sim 10^{8.6} M_{\odot}$ . The median transverse distance between the LAEs and the quasar sightlines is 165 proper kpc (pkpc). We stacked the high-resolution quasar spectra and measured significant excess H I and C IV absorption near the LAEs out to 500 km s $^{-1}$  and at least  $\approx 250$  pkpc (corresponding to  $\approx 7$  virial radii). At  $\lesssim 30$  km s $^{-1}$  from the galaxies, the median H I and C IV optical depths are enhanced by an order of magnitude. The absorption is significantly stronger around the  $\approx 1/3$  of our LAEs that are part of ‘groups’, which we attribute to the large-scale structures in which they are embedded. We do not detect any strong dependence of either the H I or C IV absorption on transverse distance (over the range  $\approx 50$ –250 pkpc), redshift, or the properties of the Ly  $\alpha$  emission line (luminosity, full width at half-maximum, or equivalent width). However, for H I, but not C IV, the absorption at  $\lesssim 100$  km s $^{-1}$  from the LAE does increase with the SFR. This suggests that LAEs surrounded by more H I tend to have higher SFRs.

**Key words:** galaxies: haloes – galaxies: high-redshift – intergalactic medium – quasars: absorption lines.

## 1 INTRODUCTION

The circumgalactic medium (CGM) is the reservoir of gas and metals in the immediate vicinity of galaxies. The physical and chemical properties of the CGM retain imprints of gas infall and outflow processes that regulate galaxy evolution. Owing to its extremely low density, direct detection of the bulk of the CGM in emission is not yet possible. However, it has recently become feasible to study the densest part of the CGM of high-redshift galaxies. For example, extended Ly  $\alpha$  emission is detected over a few tens of kpc around normal  $z > 3$  Ly  $\alpha$  emitting galaxies (e.g. Wisotzki et al. 2016; Leclercq et al. 2017) and over a few hundreds of kpc around quasar host galaxies (e.g. Cantalupo et al. 2014; Borisova et al. 2016; Cai et al. 2019), a protocluster (Umehata et al. 2019), and groups of Ly  $\alpha$  emitters (Bacon et al. 2021).

Absorption line spectroscopy of bright background sources (usually quasars) is a proven technique to probe the diffuse circumgalactic gas (see Tumlinson, Peeples & Werk 2017, for a review). Thanks

to the Cosmic Origins Spectrograph (COS) onboard *Hubble Space Telescope*, it is now well-established that the metal-enriched, ionized, multiphase CGM harbours gas and metal masses that are at least comparable to those in galaxies themselves and can potentially account for the ‘missing baryons’ and ‘missing metals’ in low- $z$  galaxies (e.g. Tumlinson et al. 2011; Peeples et al. 2014; Werk et al. 2014; Johnson et al. 2017; Keeney et al. 2017).

Despite the availability of a large repository of high-resolution, optical spectra of high- $z$  quasars (e.g. O’Meara et al. 2015; Murphy et al. 2019), CGM studies at high- $z$  have been more limited. This is primarily because detecting typical high- $z$  galaxies is challenging owing to their relative faintness.

On large scales, cross-correlation analyses between H I, traced by the Ly  $\alpha$  forest absorption, and high- $z$  galaxies have been carried out (e.g. Adelberger et al. 2005; Crighton et al. 2011; Bielby et al. 2017; Mukae et al. 2017). Crighton et al. (2011) reported an excess H I absorption within  $\approx 5h^{-1}$  comoving Mpc (cMpc $^{-1}$ ) of  $z \approx 3$  Lyman break Galaxies (LBGs). The spatial correlation between photo- $z$

\* E-mail: [sowgat@iucaa.in](mailto:sowgat@iucaa.in)

<sup>1</sup>For physical (comoving) distances we use the prefix ‘p’ (‘c’) before the unit.

galaxies and Ly $\alpha$  forest absorption lines have been studied at  $z \approx 2-3$  by Mukae et al. (2017). They reported a positive correlation between galaxy overdensities and Ly $\alpha$  forest absorption lines in space, which indicates that high- $z$  galaxies are surrounded by an excess of H I gas. Momose et al. (2021) performed a cross-correlation analysis between 570 galaxies with spectroscopic redshifts and the Ly $\alpha$  forest transmission at  $z \approx 2.3$  and found a correlation out to  $50 h^{-1}$  cMpc. In addition, they showed that the signal varies with the galaxy population, depending on scale. For scales  $r > 5 h^{-1}$  cMpc, the strongest signals are exhibited by active galactic nuclei (AGNs) and submillimetre galaxies (SMGs). Ly $\alpha$  emitters (LAEs), on the contrary, are more strongly correlated with the absorption on small scales ( $r < 5 h^{-1}$  cMpc). Bielby et al. (2020) detected LAEs within 250 pkpc and  $1000 \text{ km s}^{-1}$  of six out of nine strong absorption systems at redshift 4–5, which they showed implies the absorbers are associated with galaxy overdensities.

The bulk of the information on the CGM at  $z \approx 2-3$  comes from the Keck Baryonic Structure Survey (KBSS) of ultraviolet (UV)-colour-selected LBGs (e.g. Adelberger et al. 2005; Steidel et al. 2010; Rakic et al. 2012; Rudie et al. 2012, 2019; Turner et al. 2014; Chen et al. 2020). In a pioneering work, Steidel et al. (2010) demonstrated that the composites of background galaxy spectra can be used to characterize the CGM. They presented the dependence of Ly $\alpha$  and other metal line (e.g. Si II, Si IV, and C IV) absorption on the galactocentric radius (impact parameter,  $\rho$ ) out to 125 pkpc using 512 close foreground-background angular pairs constructed of 89 LBGs from the KBSS survey.

Using 679 KBSS galaxies probed by 15 background quasars, Rakic et al. (2012) produced the first 2D maps of Ly $\alpha$  absorption as a function of impact parameter and velocity difference around high- $z$  star-forming galaxies by stacking the quasars' spectra. They found that the median Ly $\alpha$  optical depth around LBGs is enhanced compared to randomly chosen regions out to hundreds of kpc. From a comparison to hydrodynamical simulations, Rakic et al. (2013) showed that hydrodynamical simulations can reproduce the data if the LBGs reside in haloes of mass  $M_h \sim 10^{12} M_\odot$ , a mass consistent with estimated based on galaxy clustering (Trainor & Steidel 2012).

Rudie et al. (2012) performed Voigt profile decomposition of the full Ly $\alpha$  forest region of the same 15 quasars, and studied the absorber–galaxy connection. They found that nearly half of the strong H I absorbers with column density  $N(\text{H I}) > 10^{15.5} \text{ cm}^{-2}$ , arise from the CGM, which they defined as the region with  $\rho < 300$  pkpc and within  $\pm 300 \text{ km s}^{-1}$  of galaxy's systemic redshift. The median Doppler parameters for the CGM absorbers were found to be larger than for randomly chosen absorbers, which they attributed to accretion shocks and galactic winds around the LBGs.

Using a sample of 854 KBSS galaxies (35 with  $\rho < 250$  pkpc) as well as a subsample of 340 objects with accurate redshifts based on nebular emission lines, Turner et al. (2014) confirmed the results of Rakic et al. (2012) for H I and demonstrated that the detected redshift space distortions are robust to redshift errors. They also produced the first 2D maps of the distribution of metal ions, finding a strong enhancement of absorption relative to random regions for C III, C IV, Si IV, and O VI, which extends out to at least 180 pkpc in the transverse direction and  $\pm 240 \text{ km s}^{-1}$  along the line of sight (LOS). The absorption signals for H I and C IV extend to 2 pMpc in the transverse direction, corresponding to the maximum impact parameter in their sample. Turner et al. (2017) compared the results for H I, C IV, and Si IV to the EAGLE simulation (Schaye et al. 2015), finding excellent agreement, and showed that in EAGLE the redshift-space distortions detected for impact parameters similar to the virial radii are due to infall rather than outflows. Turner et al. (2015)

presented a statistical detection of O VI near the KBSS galaxies that is not associated with significant H I and extends out to velocities exceeding the virial velocity, suggesting the presence of fast, hot and metal-rich outflows.

Recently, Chen et al. (2020) have extended the sample of Steidel et al. (2010) to  $\sim 200\,000$  pairs, and presented a 2D apparent Ly $\alpha$  optical depth map as a function of LOS velocity ( $v_{\text{LOS}}$ ) and impact parameter, finding results consistent with Turner et al. (2014). They reported a significant asymmetry for  $50 \lesssim \rho(\text{pkpc}) \lesssim 200$  and  $200 \lesssim |v_{\text{LOS}}|(\text{km s}^{-1}) \lesssim 500$ , and argued that contamination of the Ly $\alpha$  absorption by extended, diffuse Ly $\alpha$  emission from the foreground galaxy is the most likely reason for the asymmetry. Studies with much brighter background sources, such as quasars, will, however, not be affected by such phenomena. A simple, two-component analytical model with purely radial inflow and outflow can reproduce the overall features of the observed map. The model suggests that outflows dominate in the inner parts ( $\rho \lesssim 50$  pkpc), whereas inflows dominate the outer regions ( $\rho \gtrsim 100$  pkpc) of the CGM. This leads to a sudden dip in the Ly $\alpha$  rest-frame equivalent width ( $W_r$ ) profile, which otherwise can be approximated as a power law with a slope of  $-0.4$ .

None of these studies have explored whether the diffuse circumgalactic gas shows any trend with the properties of the host galaxies such as the star formation rate (SFR). Moreover, the KBSS is limited to relatively massive ( $M_h \sim 10^{12} M_\odot$ ) galaxies at  $z \approx 2-3$  with  $\text{SFR} \gtrsim 10 M_\odot \text{ yr}^{-1}$ . Such objects represent the tip of the iceberg of the typical high- $z$  galaxy population, which is difficult to probe with broad/narrow-band colour selection techniques such as used by the KBSS.

With the advent of powerful IFUs such as the Multi Unit Spectroscopic Explorer (MUSE; Bacon et al. 2010) on the Very Large Telescope (VLT), it is now possible to achieve high spectroscopic completeness of faint galaxies. The high throughput (35 per cent at around  $7000 \text{ \AA}$ ), large 1 arcmin  $\times$  1 arcmin field of view (FoV), and 0.2 arcsec per pixel spatial sampling of MUSE are ideally suited to identify foreground galaxies around bright background quasars. MUSE allows one to find galaxies and obtain their redshifts simultaneously. Most importantly, galaxies that are too faint to be detected in the continuum emission can still be picked up through their line emission. For example, the continuous spectral coverage of  $4750-9350 \text{ \AA}$  in the nominal mode of MUSE allows one to detect Ly $\alpha$  emission from galaxies in the redshift range  $\approx 2.9-6.6$  (see Fig. 1). Therefore, MUSE fields around bright high- $z$  quasars with high-quality optical spectra provide a new opportunity to probe the connection between low-mass galaxies and their gaseous environments at  $z > 3$ . Using  $\approx 50$  h of MUSE guaranteed time observations, we present here the first statistical study of the CGM of  $96 z \approx 3.3$ , low-mass ( $M_h \sim 10^{11} M_\odot$ ), star-forming ( $\leq 1 M_\odot \text{ yr}^{-1}$ ) Ly $\alpha$  emitting galaxies. We note here that a number of studies in the literature performed the reverse experiment, i.e. searched for LAEs around different types of absorbers such as C IV absorbers (Díaz et al. 2015, 2021; Zahedy et al. 2019), Lyman limit systems (Fumagalli et al. 2016; Lofthouse et al. 2020; Nielsen et al. 2020), and damped Ly $\alpha$  absorbers (Mackenzie et al. 2019) using narrow-band/long-slit/IFU spectroscopy but only for a handful of systems.

The LAEs whose CGM is probed here are detected in eight MUSE fields, centred on eight high- $z$  quasars, as part of the MUSE Quasar-field Blind Emitters Survey (MUSEQuBES; Muzahid et al. 2020). Since MUSE allows us to detect LAEs only at  $z > 2.9$ , the redshift of the background quasars must be  $> 2.9$  in order to probe the CGM of the foreground LAEs. For redshift  $z > 4$ , the Ly $\alpha$ -forest absorption in quasar spectra become too severe for accurate measurements of

Ly  $\alpha$  equivalent widths and/or column densities. When constructing our sample, we thus restrict ourselves to UV-bright quasars ( $V < 19$ ) in the redshift range 3.5–4.0 that are accessible with the VLT. We finally chose eight UV-bright quasars in the redshift range 3.6–3.9 for which significant amounts of data were already available in the public archive, which we, however, augmented with new VLT/UVES observations, yielding  $\approx 250$  h of UVES data in total. The LAEs in our sample thus have redshifts in the range 2.9–3.9. For this redshift range, night-sky emission lines have only a minimal impact in the corresponding Ly  $\alpha$  observed wavelength range (4750–5960 Å). Minimizing the effects of sky-line contamination is crucial for correctly identifying galaxies that are detected via standalone emission line such as the Ly  $\alpha$  line for  $z > 3$  LAEs.

Using the LAE sample from the MUSEQuBES survey, we showed in Muzahid et al. (2020) that the stacked CGM absorption can be used to calibrate the Ly  $\alpha$  redshifts, at least statistically, as first done for KBSS galaxies by Rakic et al. (2011). This is important, because Ly  $\alpha$  lines are known to be affected by resonant scattering. Here, we used the empirical calibration from Muzahid et al. (2020) to correct the Ly  $\alpha$  redshifts, and subsequently study the trends between the LAE properties and the stacked CGM absorption. This paper is organized as follows: In Section 2, we describe the MUSE and UVES/HIRES observation details and data reduction procedures. In Section 3, we describe the MUSE data analysis and the LAE sample, followed by the pixel optical depth recovery from the quasar spectra. The main results of this study are presented in Section 4. These findings are discussed in the context of existing results from the literature in Section 5. Finally, a summary of the paper is presented in Section 6. Throughout this study, we adopt a flat  $\Lambda$ CDM cosmology with  $H_0 = 70 \text{ km s}^{-1} \text{ Mpc}^{-1}$ ,  $\Omega_m = 0.3$ , and  $\Omega_\Lambda = 0.7$ .

## 2 OBSERVATIONS

### 2.1 MUSE observations and data reduction

The high-redshift MUSEQuBES survey exploits  $\approx 50$  h of MUSE guaranteed time observations (GTO) centred on eight bright,  $3.6 < z < 3.9$  quasars. The MUSE data for the eight quasar fields were obtained in dark time with seeing  $< 0.9$  arcsec between period P94 and P97 over the periods of 2 yr. All fields were observed for at least 2 h and four fields have been observed for 10 h each. Each observation block of 1 h was divided into  $4 \times 900$  s exposures. We conducted the observations in the WFM-NOAO-N mode which offers excellent spatial sampling of 0.2 arcsec per (square) pixel throughout the large  $1 \text{ arcmin} \times 1 \text{ arcmin}$  FoV and spectral resolution ( $R$ ) ranging from  $\approx 1800$  (FWHM  $\approx 168 \text{ km s}^{-1}$ ) to  $\approx 3600$  (FWHM  $\approx 86 \text{ km s}^{-1}$ ) in the optical (4750–9350 Å) with a spectral sampling of 1.25 Å per pixel. Further details of the MUSE observations are given in Table 1.

The standard ESO MUSE Data Reduction Software (DRS; Weilbacher et al. 2020) was used to reduce the individual raw science frames using default (recommended) sets of parameters. The four 10 h fields Q0055–269, Q1317–0507, Q1621–0042, and Q2000–330 were reduced using pipeline version v1.6. The remaining four fields were reduced using version v2.4. First, we prepared the master calibration files (bias, dark, flat, wavelength calibration, and twilight) for all 24 IFUs and removed the instrumental signatures from the science exposures and from the standard star exposures using recipes available in the DRS. The `muse_scibasic` recipe was then used for the basic science reduction using an illumination flat-field typically observed within  $\pm 1$  h around the science exposures and using a proper geometry table. This produces the pre-reduced pixel tables for each IFUs for each science frame. Finally, the

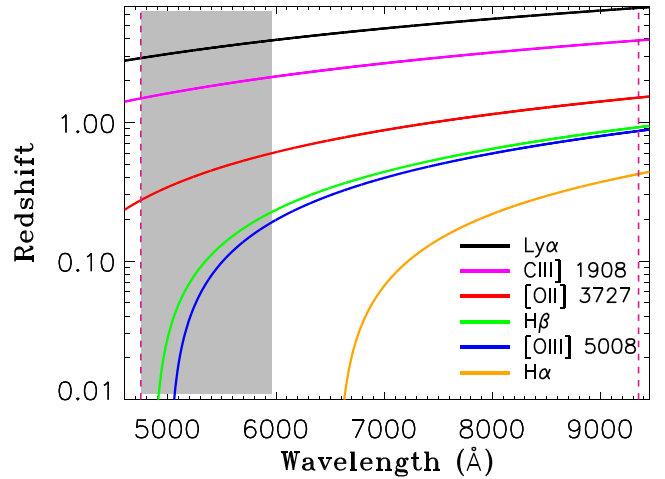


**Figure 1.** Redshift ranges covered by MUSE for different lines. The vertical dashed lines indicate the MUSE wavelength coverage in the nominal mode. We searched for LAEs in the redshift range 2.9–3.9 (below the redshifts of the background quasars). The corresponding wavelength range is indicated by the grey shaded region. The prominent emission lines from low- $z$  objects that can contaminate our LAE sample are shown. The redshifts at which a given curve enters and leaves the shaded region define the range for which the corresponding line can contaminate the LAE sample. For example, [O II] emitters between  $z = 0.27$  and  $0.52$  are potential contaminants for our sample. Note that low- $z$  H  $\alpha$  emitters cannot contaminate our sample.

`muse_scipost` recipe was used to merge all the pixel tables from all IFUs using the proper astrometry table. Flux calibration was done during this step using the response curve and telluric absorption correction from a spectrophotometric standard star observed during the same night.

In order to minimize the impact of bad pixels and cosmic rays, two subsequent science exposures were taken with small offsets ( $< 1$  arcsec) and  $90^\circ$  rotation. Note that a small frame-to-frame spatial offset can also occur owing to a ‘derotator wobble’ (Bacon et al. 2015). Different frames thus do not cover the exact same sky location. The `muse_exp_align` recipe was used to automatically compute the offsets among the exposures, and then to apply the correction to the reduced pixel tables. The reduced offset-corrected pixel tables were then used to obtain the reduced, flux-calibrated data drizzled on to a 3D (ra, dec,  $\lambda$ ) grid.

We did not use the default auto/self-calibration and sky-subtraction recipes offered by the DRS. Instead, we used the `CubeFix` and `CubeSharp` routines within CUBEX (v1.6) software developed by Cantalupo et al. (2019) for self-calibration and sky-subtraction since they provide a better final data product in terms of both illumination and flux homogeneity compared to the standard pipeline (see e.g. fig. 1 of Lofthouse et al. 2020). We refer the reader to section 2.3 of Borisova et al. (2016) for details about the self-calibration and sky-subtraction using CUBEX. The illumination corrected and sky-subtracted cubes are then combined using an average  $3\sigma$ -clipping algorithm using the `CubeCombine` routine available within CUBEX. In order to further improve the illumination correction, we iterated the above steps after masking the bright continuum objects detected in the white-light image created from the initial combined cube. As noted by Borisova et al. (2016), typically one iteration is sufficient for adequate improvement before the individual cubes can be combined to obtain the final, science-ready data product.

The effective seeing, obtained from fitting a Moffat profile to a point source at  $\lambda \approx 7000$  Å, of the final data cubes varies between

**Table 1.** Summary of UVES and MUSE observations.

Quasar field	RA <sub>QSO</sub> (hh:mm:ss)	Dec <sub>QSO</sub> (dd:mm:ss)	z <sub>QSO</sub>	V	UVES observations	t <sub>UVES</sub> (h)	MUSE observations	t <sub>MUSE</sub> (h)	Seeing (arcsec)
(1)	(2)	(3)	(4)	(5)	(6)	(7)	(8)	(9)	(10)
Q1422+23 <sup>a</sup>	14:24:38.09	+22:56:00.59	3.631	15.84	091.A-0833(A) <sup>a</sup>	5.4	60.A-9100(B) <sup>b</sup>	1.0	0.77
					093.A-0575(A) <sup>a</sup>	7.1	095.A-0200(A) <sup>a</sup>	3.0	
							099.A-0159(A) <sup>a</sup>	1.0	
Q0055–269 <sup>a</sup>	00:57:58.02	–26:43:14.75	3.662	17.47	65.O-0296(A) <sup>c</sup>	26.1	094.A-0131(B) <sup>a</sup>	3.0	0.72
					092.A-0011(A) <sup>a</sup>	21.0	096.A-0222(A) <sup>a</sup>	7.2	
Q1317–0507	13:20:29.97	–05:23:35.37	3.700	16.54	075.A-0464(A) <sup>d</sup>	13.4	095.A-0200(A) <sup>a</sup>	4.0	0.62
					093.A-0575(A) <sup>a</sup>	21.7	096.A-0222(A) <sup>a</sup>	4.0	
							097.A-0089(A) <sup>a</sup>	2.0	
Q1621–0042	16:21:16.92	–00:42:50.91	3.709	17.97	075.A-0464(A) <sup>d</sup>	15.6	095.A-0200(A) <sup>a</sup>	4.8	0.64
					091.A-0833(A) <sup>a</sup>	27.5	097.A-0089(A) <sup>a</sup>	5.0	
					093.A-0575(A) <sup>a</sup>	5.0			
QB2000–330 <sup>a</sup>	20:03:24.12	–32:51:45.14	3.783	18.40	65.O-0299(A) <sup>e</sup>	1.0	094.A-0131(B) <sup>a</sup>	10.0	0.73
					166.A-0106(A) <sup>f</sup>	40.0			
PKS1937–101 <sup>a</sup>	19:39:57.26	–10:02:41.52	3.787	19.00	077.A-0166(A) <sup>g</sup>	15.0	094.A-0131(B) <sup>a</sup>	3.0	0.81
							197.A-0384(C) <sup>h</sup>	1.9	
J0124+0044	01:24:03.78	+00:44:32.74	3.840	18.71	69.A-0613(A) <sup>i</sup>	1.0	096.A-0222(A) <sup>a</sup>	2.0	0.83
					71.A-0114(A) <sup>i</sup>	1.0	197.A-0384(D) <sup>h</sup>	1.6	
					073.A-0653(C) <sup>j</sup>	3.3			
					092.A-0011(A) <sup>a</sup>	35.6			
BRI1108–07 <sup>a</sup>	11:11:13.60	–08:04:02.00	3.922	18.10	67.A-0022(A) <sup>c</sup>	1.3	095.A-0200(A) <sup>a</sup>	2.0	0.72
					68.B-0115(A) <sup>k</sup>	7.7	197.A-0384(C) <sup>h</sup>	2.4	
					68.A-0492(A) <sup>c</sup>	5.6			

*Notes.* (1) Name of the quasar field. (2) Quasar right ascension (J2000). (3) Quasar declination (J2000). (4) Quasar redshift (5). Quasar V-band magnitude. (6) PID of UVES observations. (7) UVES exposure time. (8) PID of MUSE observations. (9) MUSE exposure time of the field. (10) Seeing (Moffat FWHM) of the final coadded data cube at around 7000 Å. Columns 2–5 are obtained from SIMBAD (<https://cds.u-strasbg.fr/>) data base. <sup>a</sup>PI: Schaye. <sup>b</sup>MUSE Commissioning data – not used in this study. <sup>c</sup>PI: D’Odorico. <sup>d</sup>PI: Kim. <sup>e</sup>PI: D’Odorico, V. <sup>f</sup>PI: Bergeron. <sup>g</sup>PI: Carswell. <sup>h</sup>PI: Fumagalli; data not used in this study. <sup>i</sup>PI: Péroux. <sup>j</sup>PI: Bouché. <sup>k</sup>PI: Molaro. <sup>α</sup>Keck/HIRES data available.

0.62 and 0.83 arcsec. The wavelengths in the MUSE data cubes are given in air. However, all redshifts given in this work correspond to vacuum redshifts, as we apply the appropriate air-to-vacuum corrections while building the LAE catalogue.

## 2.2 UVES and HIRES observations and data reduction

As mentioned in Section 1, the eight quasars chosen in this survey already had exquisite quality optical spectra with spectral resolution,  $R \approx 45\,000$  obtained with the VLT/UVES (and Keck/HIRES) that were publicly available. However, sometimes the existing spectra did not cover the full wavelength range required for this study. For five out of eight quasars, we augmented the existing data with new observations in order to fill in spectral gaps and/or to improve the signal-to-noise ratio ( $S/N$ ). The spectral coverage and  $S/N$  of the remaining three quasar spectra were sufficient for this study except for PKS1937–101, for which we have spectral coverage up to 6813 Å, whereas the C IV region extends out to 7493 Å. Column 6 of Table 1 lists the proposal identifiers (PIDs) under which the data were taken. We checked the title of the each program and found that only two quasars (J 0124+0044 and BRI1108–07) were observed because of the presence of damped Ly $\alpha$  absorbers (DLAs) in their spectra.

The ancillary VLT/UVES data for the five quasars were obtained in ESO periods P91–P93 in grey/dark time ( $\approx 123$  h in total) with a seeing  $\approx 1$  arcsec (PI: Schaye). A slit width of 1 arcsec was used

for these observations yielding a spectral resolution  $R \sim 40\,000$ . Except for the quasar Q1422+23, the final coadded and continuum-normalized spectra were downloaded from the SQUAD data base (Murphy et al. 2019).<sup>2</sup> The raw frames of the quasar Q1422+23 were reduced using the COMMON PIPELINE LANGUAGE (CPL v6.3) of the UVES pipeline. After the initial reduction, we used the UVES POPLER<sup>3</sup> software to combine the extracted Echelle orders into a single 1D spectrum. Note that the spectra in the SQUAD data base are also generated using UVES POPLER. Continuum normalization of the final coadded spectrum was done by fitting smooth low-order spline polynomials in line-free regions determined by iterative sigma-clipping.

Finally, Keck/HIRES data are available for five out of eight quasars (see Table 1). Since the  $S/N$  of the UVES spectra (Table 2) are more than sufficient for the stacking exercise presented here, we generally did not use the HIRES spectra except for two quasars. We used the HIRES spectra of PKS1937–101 (PIs: Cowie, Crighton, Tytler) and Q1422+23 (PIs: Cowie, Sargent) from the KODIAQ data release (O’Meara et al. 2015) to fill in the gaps in the UVES spectra. The continuum-normalized UVES and HIRES spectra are combined using inverse-variance weighting.

<sup>2</sup>The spectrum of the quasar Q1422+23 was not available in the SQUAD repository.

<sup>3</sup><https://doi.org/10.5281/zenodo.44765>

**Table 2.** Spectral coverage and  $S/N$  of the quasar spectra.

Quasar	$\lambda_{\min}^a$	$\lambda_{\max}^b$	$S/N_{5230 \text{ \AA}}^c$	$S/N_{6660 \text{ \AA}}^d$
Q1422+23	3400	7290	174	194
Q0055–269	3140	9767	41	80
Q1317–0507	3238	9467	36	96
Q1621–0042	3735	9467	50	103
QB2000–330	4152	10 432	72	68
PKS1937–101	4000	6813	77	86
J0124+0044	3700	9467	28	71
BRI1108–07	4394	10 429	14	24

*Notes.* <sup>a</sup>The minimum wavelength (in  $\text{\AA}$ ) covered by the spectrum. <sup>b</sup>The maximum wavelength (in  $\text{\AA}$ ) covered by the spectrum. <sup>c</sup>The median  $S/N$  per pixel calculated at  $5230 \pm 50 \text{ \AA}$ . <sup>d</sup>The median  $S/N$  per pixel calculated at  $6660 \pm 50 \text{ \AA}$ . The  $S/N$  are calculated at the expected wavelengths of  $\text{Ly}\alpha$  and C IV, respectively, for the median redshift of 3.3 of the survey.

### 3 DATA ANALYSIS

#### 3.1 MUSE data analysis and the LAE sample

Here, we describe the procedures for extraction and classification of objects from the final, combined MUSE data cubes obtained in Section 2.1. Different routines within the CUBEX package are used for automatic extraction of emission line sources, for extracting 1D spectra, and for measuring  $\text{Ly}\alpha$  line fluxes using the curve-of-growth method.

Before extracting emission line sources from the data cubes, we first removed the quasars’ point spread functions (PSFs). Galaxies close to the quasar LOSs (small impact parameters) are more likely to produce strong absorption in the quasar spectrum. Finding such small-impact-parameter galaxies is thus important. The essential step to finding such small-impact-parameter galaxies is to get rid of the contamination due to the quasar’s PSF. We used the `CubePSFSub` routine that determines and subtracts the PSF empirically (see section 3.1 of Borisova et al. 2016, for details). Briefly, a pseudo-narrow-band (NB) image is created for each wavelength layer at the position of the quasar with a bandwidth of 150 layers ( $\approx 187 \text{ \AA}$ ). These images are treated as the empirical PSFs of the quasar. The adopted bandwidth is a trade off between maximizing the  $S/N$  of the pseudo-NB images and minimizing the wavelength variations of the PSF. Each PSF image is then scaled to match the flux in the central  $1 \text{ arcsec} \times 1 \text{ arcsec}$  area centred on the peak of the quasar emission at that layer. This scaled empirical PSFs are subsequently subtracted from the corresponding layers up to 5 arcsec radius. As noted by Borisova et al. (2016), this method of PSF subtraction cannot provide any meaningful information on the central  $1 \text{ arcsec} \times 1 \text{ arcsec}$  region used for PSF rescaling which sets the lower limit on the impact parameter of  $\approx 8 \text{ pkpc}$  at  $z \approx 3$ .

In order to remove the remaining continuum emitting sources, we next used the `CubeBKSub` routine within the CUBEX package (see section 3.2 of Borisova et al. 2016, for details). In brief, the spectrum of each spaxel of the PSF-subtracted cube is first binned using a bin size of 40 layers ( $\approx 50 \text{ \AA}$ ). This resampled spectrum is then smoothed with a median filter with a size of three bins (radius). The smoothed cube is subsequently subtracted from the original cube.

Finally, we run CUBEX (v1.6) on the continuum-subtracted cube for automatic extraction of emission line sources. First the datacube and its associated variance are filtered (smoothed) by a Gaussian kernel with a size of 2 pixels (radius) at each wavelength layer. The contiguous voxels with  $S/N > 4$  are then grouped together. Following

Marino et al. (2018), a group of  $>40$  connected voxels is regarded a detection. In addition, we require a spectral  $S/N > 4.5$  measured on the 1D  $\text{Ly}\alpha$  emission line spectrum for an unambiguous detection. The voxels that are part of a group satisfying these conditions are used to create a 3D segmentation map (object mask). This segmentation map is subsequently used for extracting 1D spectra and for creating pseudo-NB images around the emission features. We typically masked the noisy pixels (up to 20 pixels) at the edge of the field. We also masked the first eight wavelength layers of each cube and about 10 wavelength layers near the two strong skylines at  $\approx 5578$  and  $\approx 5895 \text{ \AA}$  to suppress the number of spurious detections. Note that we only search for emitters with redshifts lower than the redshift of the background quasar, by masking the wavelengths redwards of the  $\text{Ly}\alpha$  emission.

Proper characterization of the noise is crucial for any source extraction procedure based on  $S/N$  threshold. The detector noise propagated through different reduction steps cannot fully capture the correlated noise introduced by resampling and interpolation. The propagated variance produced by the MUSE pipeline and subsequently post-processed by `CuBFix` and `CuBeSharp` thus underestimates the ‘true’ noise. In order to account for this, CUBEX rescales the propagated variance by a constant factor, determined from the spatial average of the propagated variance, for each wavelength layer. This rescaling factor typically varies between  $\approx 1.5$  and 2.0.

The 1D spectra and the pseudo-NB images of all the extracted objects were inspected visually. These objects were then classified by two members of the team (SM and RAM) independently. Note that building a LAE catalogue from MUSE data alone is not straightforward, since no other prominent emission lines are covered in the MUSE passband. Thus, identification of an LAE is, almost always, solely based on the  $\text{Ly}\alpha$  emission. This is particularly problematic for weak lines. The strong lines usually show the characteristic asymmetric profile with an occasional blue bump, and are therefore easy to classify. An example of such a strong  $\text{Ly}\alpha$  emitter is shown in the top panel of Fig. 2. However, as shown in the bottom panel, it is not always straightforward, particularly for the weaker lines. We followed a ‘method of elimination’ as our strategy to classify  $\text{Ly}\alpha$  emitters in such cases. We consider all the different possible redshift solutions for a given emitter and eliminate them systematically until we find the best/most likely solution. As demonstrated in Fig. 1, there are several prominent emission lines (e.g. C III]  $\lambda\lambda 1907, 1909$ , [O II]  $\lambda\lambda 3727, 3729$ , H $\beta$   $\lambda 4862$ , and [O III]  $\lambda 5008$ ) that can contaminate our LAE sample. It is known that the [O II]  $\lambda\lambda 3727, 3729$  doublet from low- $z$  objects is the major contaminant for high- $z$  LAE samples. The [O II] emitters in the redshift range 0.27–0.52 are potential contaminants for our sample (see Fig. 1). Nevertheless, the doublet nature of the [O II] line provides important clues. In addition, other strong emission lines such as [O III], H $\beta$ , and/or H $\alpha$  are always covered by MUSE for an [O II] emitter in the redshift range 0.27–0.52. The presence or absence of additional lines helps tremendously to distinguish an [O II] emitter from an LAE (e.g. Inami et al. 2017).

In total, we classified 96 objects as  $\text{Ly}\alpha$  emitters. For each LAE we measured the peak redshift ( $z_{\text{peak}}$ ), impact parameter ( $\rho$ ), line luminosity ( $L(\text{Ly}\alpha)$ ), full width at half-maximum (FWHM), UV luminosity ( $L_{\text{UV}}$ ), SFR, and rest-frame equivalent width ( $EW_0$ ) as discussed in detail in section 3 of Muzahid et al. (2020). Briefly, the  $z_{\text{peak}}$  and FWHM are measured directly from the 1D spectrum. The red peak is used in case of a double-peaked  $\text{Ly}\alpha$  profile. We did not apply any modelling to the emission line profile, since  $\text{Ly}\alpha$  is not well behaved owing to its resonant nature. The FWHM values are not corrected for instrumental broadening. The  $L(\text{Ly}\alpha)$  is

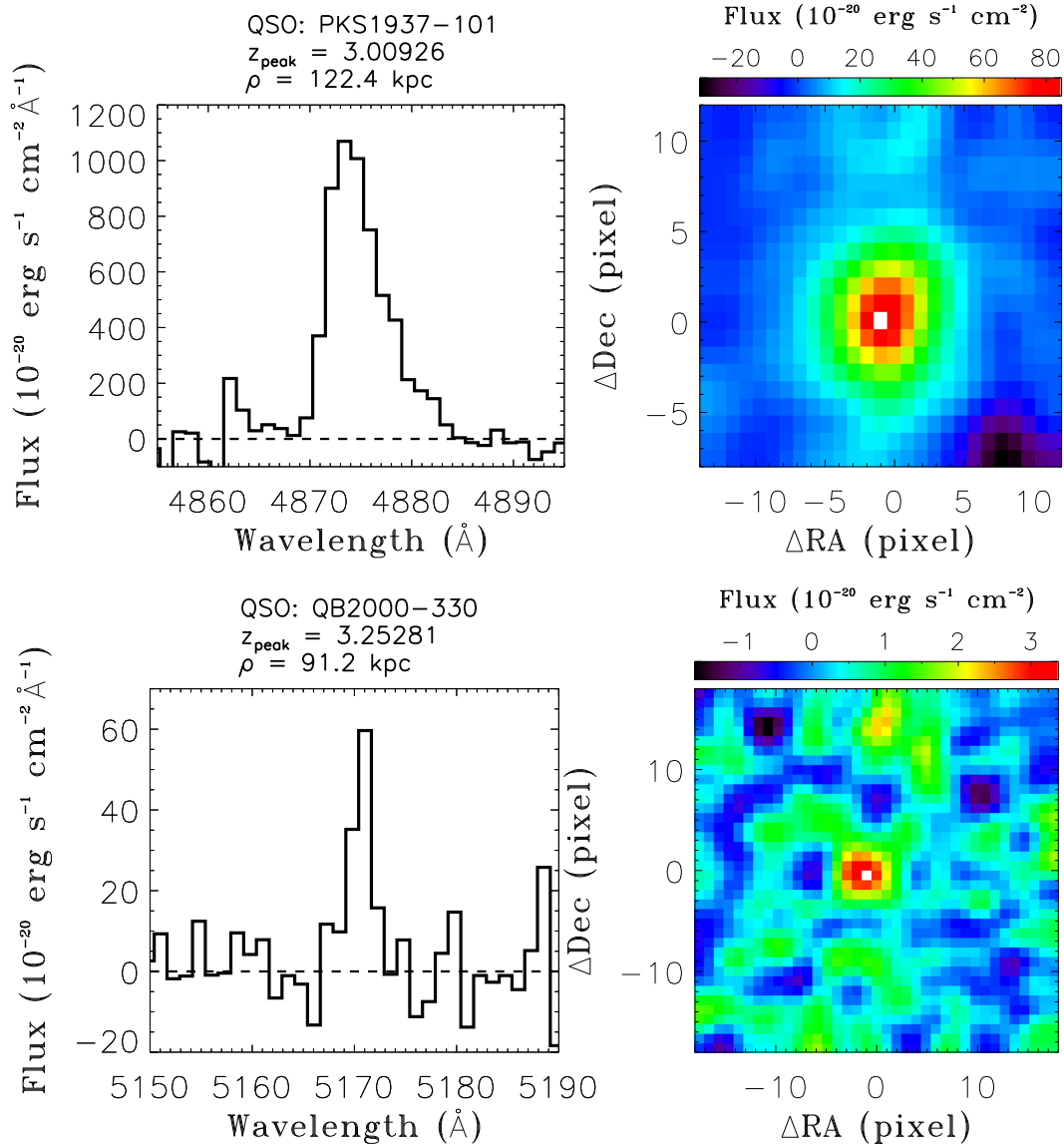


**Figure 2.** Top left: Ly $\alpha$  emission from an object detected at  $z_{\text{peak}} = 3.00926$  at an impact parameter of 122.4 pkpc towards quasar PKS 1937–101. The asymmetric profile with a prominent red wing as seen here is an unambiguous feature of Ly $\alpha$  emitters. Top right: The pseudo-NB image, smoothed by 3 pixels, of the LAE in the left. Bottom: The bottom panels show another example of an LAE with weak Ly $\alpha$  emission. In such cases, we adopted a ‘method of elimination’ as our LAE classification strategy (see text).

calculated from the Galactic extinction corrected line flux,  $f(\text{Ly}\alpha)$ , determined from the pseudo-NB images using the curve-of-growth method following Marino et al. (2018). Briefly, the total Ly $\alpha$  flux was determined from the direct sum of 0.2 arcsec annular fluxes out to the radius where the annular flux is equal to or less than zero.

The  $L_{\text{UV}}$  is calculated from the Galactic extinction-corrected UV continuum flux, determined by direct integration of the 1D spectrum between 1410 and 1640 Å (FWHM of the *GALEX* far-UV transmission curve) in the rest frame. The dust-uncorrected SFRs are calculated from the  $L_{\text{UV}}$  using the local calibration relation of Kennicutt (1998) corrected to the Chabrier (2003) stellar initial mass function. Lastly,  $EW_0$  is calculated by dividing  $f(\text{Ly}\alpha)$  by the continuum flux density, estimated by extrapolating the rest-frame 1500 Å continuum assuming a spectral index of  $-2.0$ , and correcting for the  $1 + z_{\text{peak}}$  factor. Note that the UV continuum is detected for only 39 LAEs with  $>5\sigma$  significance. For 42 LAEs, we could only

place conservative ( $5\sigma$ ) upper limits. The remaining 15 objects are blended with low- $z$  continuum sources.

### 3.2 Pixel optical depth recovery from the quasar spectra

The spectral coverage and  $S/N$  of the optical spectra (FWHM  $\approx 6.6 \text{ km s}^{-1}$ ) of the quasars are given in Table 2. The  $S/N$  per pixels ranges from 14 to 174 (24 to 194) in the blue (red) part, indicating that these are some of the best quality optical spectra of quasars ever observed. We searched for CGM absorption in the composite spectra constructed from these high-quality quasar spectra.

Before we stack the quasar spectra, we run PODPY,<sup>4</sup> a PYTHON module developed by Turner et al. (2014) to recover (from saturation

<sup>4</sup>The code is available at <http://github.com/turnerm/podpy>.

and contamination) the correct pixel optical depths (PODs) for a given transition from each spectrum (e.g. Cowie & Songaila 1998; Schaye et al. 2003; Aguirre et al. 2008). The pixel optical depth is a measure of absorption strength, and is defined as  $\tau_\lambda = -\ln(F_\lambda)$ , where  $F_\lambda$  is the continuum normalized flux of a given pixel. We used the default set of parameters used in Turner et al. (2014), which is optimized for high- $z$  quasar spectra. We refer the reader to appendix A of Turner et al. (2014) for a detailed discussion. Briefly, PODPY iteratively examines whether the optical depth of a given pixel in a spectrum is consistent with being the transition of interest. First, we set  $\tau_\lambda = 10^{-6}$  for pixels with  $F_\lambda > 1$ . The saturated pixels with  $F_\lambda \leq 3\sigma_\lambda$ , where  $\sigma_\lambda$  is the error in the normalized flux, on the contrary, are set to a very high optical depth of  $10^4$ . Note that this flag affects neither the mean nor the median flux. It also does not affect the median optical depth provided it is smaller than  $10^4$ .

For Ly  $\alpha$ , the main source of error comes from the line saturation. PODPY takes advantage of all the available Lyman series lines (up to Ly- $\lambda$ 914.9) to correct the pixel optical depths of all Ly  $\alpha$  pixels previously deemed saturated. If a correction is not possible, the Ly  $\alpha$  optical depth is set to  $10^4$ . The effect of the saturation correction is evident from the bottom panel of Fig. 3. There is a sharp cutoff at  $\tau \approx 0.5$  for the uncorrected optical depth distribution (red histogram) owing to the saturation of the Ly  $\alpha$  line. The PODPY recovered optical depth distribution does not show such a feature, with a significantly lower number of pixels flagged as saturated ( $\log_{10}\tau = 4.0$ ).

Note that we do not use the pixels in the Ly  $\beta$  forest. This sets the lower limit on redshift for the Ly  $\alpha$  stack as

$$z_{\min}^{\text{Ly}\alpha} = ((1 + z_{\text{qso}}) \times \lambda_{\text{Ly}\beta}) / \lambda_{\text{Ly}\alpha} - 1, \quad (1)$$

where  $\lambda_{\text{Ly}\alpha}$  and  $\lambda_{\text{Ly}\beta}$  are the rest-frame wavelengths of Ly  $\alpha$  and Ly  $\beta$ , respectively. Moreover, we do not use the proximate regions (3000 km s $^{-1}$  blueward of  $z_{\text{qso}}$ ) of the background quasar for any of the lines considered here. This sets the maximum redshift for the all transitions as

$$z_{\max} = z_{\text{qso}} - (1 + z_{\text{qso}}) \times \frac{3000}{c}, \quad (2)$$

where  $c$  is the speed of light in vacuum in km s $^{-1}$ . 83/96 LAEs in our sample satisfy these redshift bounds for the Ly  $\alpha$  stack. We further masked the Ly  $\alpha$  regions of six LAEs that are showing strong H I absorption with damping wings as recommended by Turner et al. (2014). This is to avoid features dominated by few strong absorbers whose velocity spread far exceeds that resulting from the peculiar and thermal velocities of the absorbing gas.

For optical depth recovery of metal line doublets such as C IV  $\lambda\lambda$ 1548,1550, we first refit the continuum redward of the quasar's Ly  $\alpha$  emission, using the `fit_continuum` routine available within PODPY. This allows us to homogenize continuum fitting errors between different quasars. Next the algorithm checks for contamination by unrelated absorption (such as Mg II from low- $z$ ) at each pixel by testing whether the optical depth in a given pixel is higher than what is expected from the weaker member of the doublet (e.g. the  $\lambda$ 1550 transition for the C IV doublet). Next, an iterative doublet subtraction algorithm is used to remove self-contamination (i.e. eliminating any contribution from the  $\lambda$ 1550 transition). As demonstrated in the top panel of Fig. 3, the recovery of the C IV  $\lambda$ 1548 pixel optical depth is dominated by the contamination correction. While the median optical depth for the PODPY recovered distribution is somewhat lower compared to the uncorrected distribution, it reduces the absorption unrelated to the galaxies leading to a significant suppression of noise.

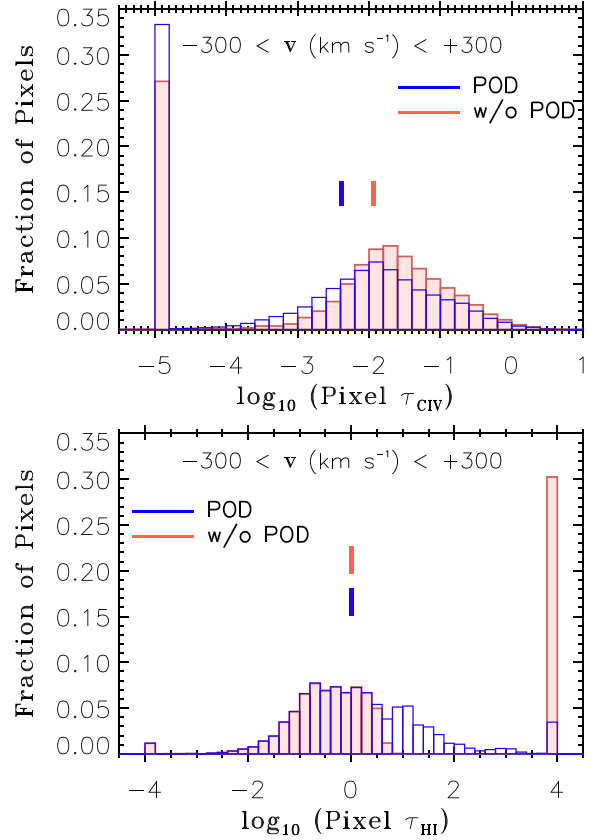


**Figure 3.** Histograms of pixel optical depths with and without POD recovery using PODPY. All pixels in the quasar spectra within  $\pm 300$  km s $^{-1}$  of  $z_{\text{peak}}$  are used in these plots. There are 77 (92) LAEs contributing to the H I (C IV) pixel optical depth distribution in the bottom (top) panel. For H I, the pixels with very high and low optical depths ( $>10^4$  and  $<10^{-4}$ ) are flagged with flag values of  $10^{+4}$  and  $10^{-4}$ , respectively. For C IV, the pixels with  $\tau > 10^1$  and  $\tau < 10^{-5}$  are flagged with flag values of  $10^{+1}$  and  $10^{-5}$ , respectively. The median values of the distributions are indicated by the vertical ticks with corresponding colours. The effect of the correction for saturation using higher order Lyman series lines by PODPY is evident from the bottom panel. The effects of the contamination correction and of rescaling the continua are apparent from the top panel.

For C IV stacks, we do not use pixels in the Ly  $\alpha$  forest region, this sets the lower limit in redshift:  $z_{\min}^{\text{C IV}} = ((1 + z_{\text{qso}}) \times \lambda_{\text{Ly}\alpha}) / \lambda_{\text{C IV}} - 1$ . All 96 LAEs in our sample satisfy the redshift bounds ( $[z_{\min}^{\text{C IV}}, z_{\max}]$ ). However, the C IV regions are affected by skylines for three LAEs ( $z = 3.455$  towards Q1317–0507,  $z = 3.453$  towards Q1621–0042, and  $z = 3.446$  towards QB2000–330). There is no spectral coverage for the  $z = 3.553$  LAE in the PKS1937–101 field. These LAEs are removed from the sample for the C IV stacks.

## 4 RESULTS

Scatter plots of the different parameters (i.e.  $\rho$ ,  $z_{\text{peak}}$ , FWHM,  $L(\text{Ly}\alpha)$ , SFR, and  $EW_0$ ) measured for the LAEs are shown in Fig. 4. The details on the measurements of these parameters are described in section 3 of Muzahid et al. (2020). There is no significant correlation between the impact parameter (ranging from 16 to 315 pkpc, median  $\rho = 165$  pkpc) and any of the other parameters. This is expected, since the impact parameter, the projected separation between the LAE and the background quasar, is not governed by any physical process

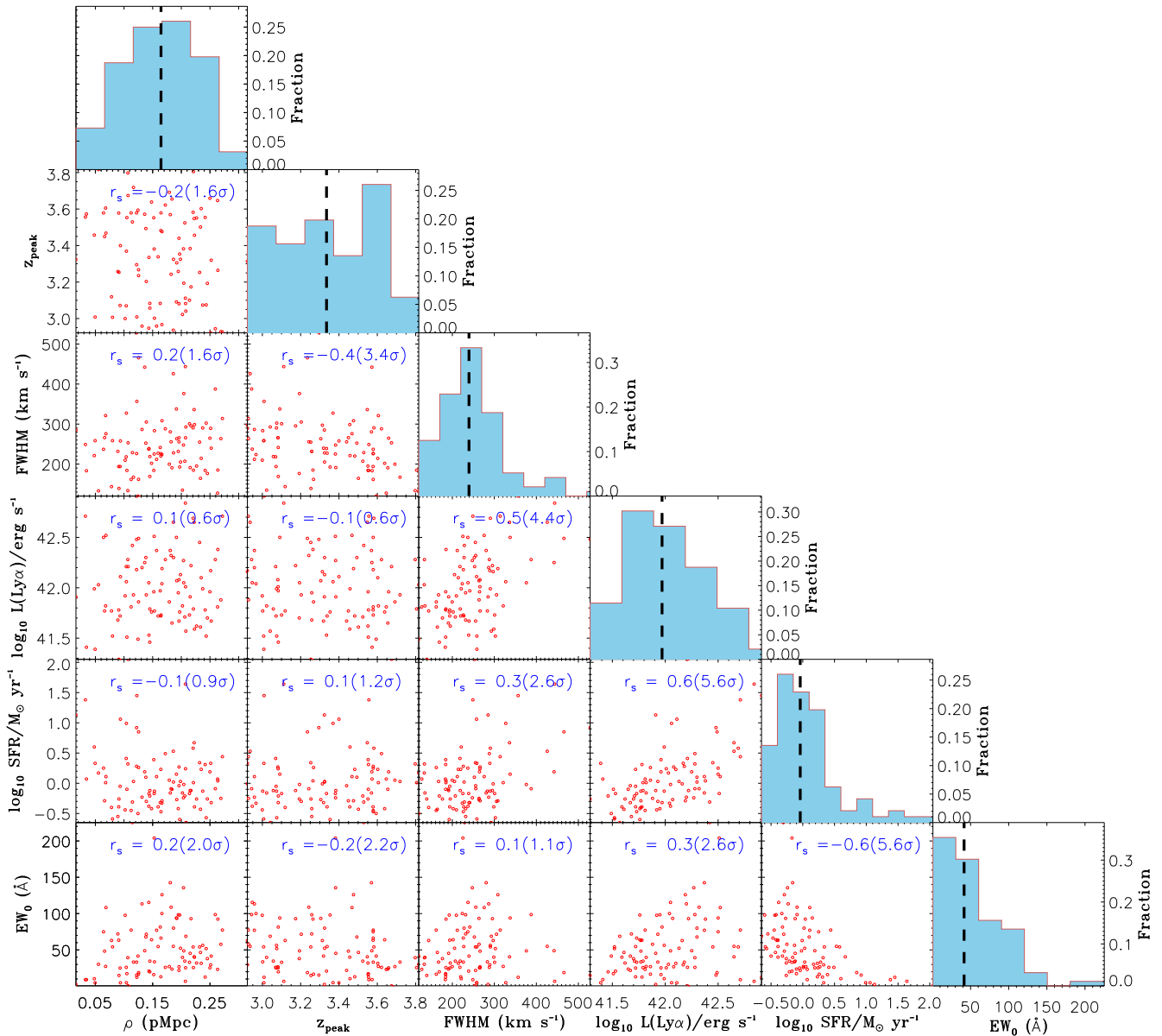


**Figure 4.** Corner plot showing possible relations between different parameters obtained for the 96 LAEs in our sample. The Spearman rank correlation coefficients ( $r_s$ ) and the corresponding significances, treating limits as detections, are indicated in each panel. The parameters showing a significant correlation with each other are discussed in the text. The vertical lines in the panels showing the relative frequency distributions indicate the corresponding median values.

in the LAE. Using Spearman rank correlation tests, no significant correlation is seen between  $z_{\text{peak}}$  (ranging from 2.9 to 3.8, median  $z_{\text{peak}} = 3.3$ ) and other parameters except for the FWHM (ranging from 120 to 528  $\text{km s}^{-1}$ , median FWHM = 240  $\text{km s}^{-1}$ ). As noted in Muzahid et al. (2020), the  $3.4\sigma$  anticorrelation between  $z_{\text{peak}}$  and FWHM is likely due to the fact that the MUSE resolution improves with wavelength (redshift) and our FWHM values are not corrected for the MUSE resolution. The FWHM also shows a significant trend with  $L(\text{Ly}\alpha)$  (ranging from  $10^{41.3}$  to  $10^{42.9}$   $\text{erg s}^{-1}$ , median  $L(\text{Ly}\alpha) = 10^{42.0}$   $\text{erg s}^{-1}$ ) which is expected since both parameters are related to the area under the emission line, provided the line is spectrally resolved.

The anticorrelation seen between SFR and  $EW_0$  follows from the fact that the SFR is directly proportional to the continuum luminosity whereas the  $EW_0$  is inversely proportional to the continuum flux

density. Finally, we notice a significant ( $5.6\sigma$ ) and strong ( $r_s = 0.6$ ) correlation between SFR and  $L(\text{Ly}\alpha)$ . This is interesting since the SFRs are calculated from the UV continuum emission, whereas  $L(\text{Ly}\alpha)$  are measured from the line emission. Owing to the resonant scattering and susceptibility to dust, the  $\text{Ly}\alpha$  line is not considered to be a good SFR indicator. The correlation between SFR and  $L(\text{Ly}\alpha)$ , none the less, suggests that the  $\text{Ly}\alpha$  line emission is dominated by the recombination radiation from atoms that were ionized by the UV photons generated via star formation activity, and that the escape fraction of  $\text{Ly}\alpha$  photons does not depend strongly on  $L(\text{Ly}\alpha)$ .

The dust-uncorrected median SFR ( $\sim 1 M_{\odot} \text{ yr}^{-1}$ ) of our sample corresponds to  $M_* \sim 10^{8.6} M_{\odot}$  for main-sequence galaxies (Behroozi et al. 2019). This is similar to the dynamical masses of the continuum-faint  $z \approx 2.5$  LAEs studied by Trainor et al. (2015), estimated assuming a spherical geometry and a radius of 0.6 kpc.

**Table 3.** List of sub/samples generated for stacking.

Sample (1)	$N_{\text{LAE}}(\text{H I})$ (2)	Median property value (3)	$N_{\text{LAE}}(\text{C IV})$ (4)	Median property value (5)
all	77	–	92	–
all_environment_iso	54	–	62	–
all_environment_group	23	–	30	–
all_ρ_low	26	$\rho = 90.8$ (49.5, 107.1) pkpc	31	$\rho = 103.8$ (64.2, 124.4) pkpc
all_ρ_mid	25	$\rho = 152.6$ (136.1, 180.7) pkpc	30	$\rho = 166.1$ (145.0, 192.0) pkpc
all_ρ_high	26	$\rho = 222.4$ (197.1, 249.9) pkpc	31	$\rho = 231.9$ (206.1, 263.3) pkpc
iso_ρ_low	18	$\rho = 78.2$ (48.1, 104.1) pkpc	21	$\rho = 93.7$ (64.2, 116.5) pkpc
iso_ρ_mid	18	$\rho = 143.5$ (122.0, 172.1) pkpc	20	$\rho = 159.5$ (138.9, 180.7) pkpc
iso_ρ_high	18	$\rho = 216.9$ (192.0, 263.3) pkpc	21	$\rho = 215.4$ (202.0, 259.3) pkpc
iso_τ <sub>peak</sub> _low	27	$\tau_{\text{peak}} = 3.254$ (3.008, 3.338)	31	$\tau_{\text{peak}} = 3.091$ (3.000, 3.295)
iso_τ <sub>peak</sub> _high	27	$\tau_{\text{peak}} = 3.553$ (3.456, 3.647)	31	$\tau_{\text{peak}} = 3.529$ (3.381, 3.647)
iso_ $L(\text{Ly}\alpha)$ _low	27	$\log_{10} L(\text{Ly}\alpha) = 41.76$ (42.52, 41.91) <sup>a</sup>	31	$\log_{10} L(\text{Ly}\alpha) = 41.76$ (41.52, 41.91) <sup>a</sup>
iso_ $L(\text{Ly}\alpha)$ _high	27	$\log_{10} L(\text{Ly}\alpha) = 42.28$ (42.06, 42.50) <sup>a</sup>	31	$\log_{10} L(\text{Ly}\alpha) = 42.28$ (42.06, 42.52) <sup>a</sup>
iso_FWHM_low	27	FWHM = 199.7 (143.6, 228.6) km s <sup>-1</sup>	31	FWHM = 199.7 (139.1, 228.6) km s <sup>-1</sup>
iso_FWHM_high	27	FWHM = 285.1 (255.5, 327.2) km s <sup>-1</sup>	31	FWHM = 292.7 (255.7, 387.6) km s <sup>-1</sup>
all_SFR_non-det	36	$\log_{10} \text{SFR} = -0.30$ (-0.50, -0.09) <sup>b, c</sup>	41	$\log_{10} \text{SFR} = -0.26$ (-0.45, -0.09) <sup>b, c</sup>
all_SFR_low	15	$\log_{10} \text{SFR} = -0.12$ (-0.32, +0.07) <sup>b</sup>	20	$\log_{10} \text{SFR} = -0.04$ (-0.26, +0.07) <sup>b</sup>
all_SFR_high	15	$\log_{10} \text{SFR} = +0.28$ (+0.19, +0.58) <sup>b</sup>	18	$\log_{10} \text{SFR} = +0.33$ (+0.19, +0.58) <sup>b</sup>
all_EW <sub>0</sub> _low	15	$EW_0 = 25.3$ (16.6, 33.2) Å	19	$EW_0 = 26.1$ (18.8, 38.0) Å
all_EW <sub>0</sub> _high	15	$EW_0 = 63.0$ (48.9, 93.0) Å	19	$EW_0 = 66.3$ (54.1, 93.0) Å

Notes. (1) List of different sub/samples generated for stacking. Except for the full sample ('all'), the name of the subsamples have three parts. The first part indicates the parent sample ('all' or 'iso') from which the subsample is created. The second part indicates the property based on which the subsample is generated (i.e. impact parameter ( $\rho$ ), Ly  $\alpha$  redshift ( $\tau_{\text{peak}}$ ), Ly  $\alpha$  line luminosity ( $L(\text{Ly}\alpha)$ ), FWHM, SFR, and Ly  $\alpha$  emission rest equivalent width ( $EW_0$ )). The third part (low/high etc.) provides the unique identifier. The 'all\_environment\_iso' is the 'isolated only' subsample. The 'all\_SFR\_non-det' is the subsample of all the UV-continuum undetected objects. (2) Number of LAEs contributing to the H I stack. (3) The median value of the property for the subsample. The values in parentheses provide the corresponding 68 percentile ranges. (4) Number of LAEs contributing to the C IV stack. (5) Same as (3) but for C IV stacks.

<sup>a</sup> $L(\text{Ly}\alpha)$  in erg s<sup>-1</sup>

<sup>b</sup>SFR in  $M_{\odot} \text{ yr}^{-1}$

<sup>c</sup>The median and 68 percentile range are calculated treating limits as detections

On such scales, the dynamical mass is likely dominated by stars. Using the abundance matching relation of Moster, Naab & White (2013), we obtain the corresponding halo mass of  $\sim 10^{11} M_{\odot}$ , and a virial radius,  $R_{200} \approx 35$  pkpc, where  $R_{200}$  is the radius at which the mean enclosed density is 200 times the critical density of the universe.

Next, we investigate possible trends between the stacked H I and C IV CGM absorption and the different properties (e.g.  $z$ ,  $\rho$ , SFR) of the LAEs discussed in the previous section. The details of the subsamples based on these properties are presented in Table 3. Note that Ly  $\alpha$  and C IV are the only two transitions for which the stacked absorption is detected at  $>3\sigma$  significance. We do not consider the higher order Lyman series lines (Ly  $\beta$  and above) in our analysis owing to the high degree of blending in the Ly  $\alpha$  forest blueward of Ly  $\beta$  emission. However, the higher order Lyman series lines are used by PODPY, whenever possible, to correct the Ly  $\alpha$  optical depths for the saturated pixels.

Since the Ly  $\alpha$  redshifts ( $z_{\text{peak}}$ ) do not represent the systemic redshifts, we obtained the corrected redshifts,  $z_{\text{corr}}$ , by blueshifting each  $z_{\text{peak}}$  value by the amount  $V_{\text{offset}}$  determined from the empirical relation (i.e.  $V_{\text{offset}} = 0.89 \times \text{FWHM} - 85$  km s<sup>-1</sup>) obtained in Muzahid et al. (2020) for our sample of LAEs. For the entire analysis presented here, we used PODPY recovered spectra to improve the continuum S/N of the stacked profiles. However, the results remain nearly unchanged if we use the original spectra instead.

#### 4.1 Pixel flux distributions

The dense Ly  $\alpha$  forest absorption seen in the spectra of high- $z$  quasars arises from both virialized haloes (i.e. the CGM of foreground galaxies) and from cosmologically evolving density fields, in the form of sheets and filaments in the intergalactic medium (IGM). In Fig. 5, we compare the pixel flux distributions of the Ly  $\alpha$  forest regions in all eight quasars to that of the CGM of 77 LAEs in our sample. For each quasar, we used fluxes in all the PODPY recovered raw spectral pixels (i.e. without binning) lying between the Ly  $\beta$  emission and 3000 km s<sup>-1</sup> bluewards of the Ly  $\alpha$  emission to determine the IGM + CGM flux distribution. For the CGM pixel flux distributions, we used  $\pm 100$  km s<sup>-1</sup> (bottom) and  $\pm 1000$  km s<sup>-1</sup> (top) velocity windows around  $z_{\text{corr}}$ .

The bottom panel of Fig. 5 shows that the CGM pixel flux distribution is significantly different from the distribution of the overall Ly  $\alpha$  forest fluxes. A two-sided Kolmogorov–Smirnov (KS) test returns  $D_{\text{KS}} = 0.39$ ,  $P_{\text{KS}} = 10^{-10}$ . The CGM pixel flux distribution shows a strong peak in the lowest flux bin, suggesting significantly stronger absorption (higher optical depth) than seen in the Ly  $\alpha$  forest regions at similar redshifts. The CGM flux distribution has a +ve skew (right-skewed) with a median flux of 0.05 which is much lower than the mean value of 0.29. The Ly  $\alpha$  forest flux distribution, on the other hand, is left-skewed with a median value (0.74) higher than the mean (0.61). Note that the mean and median values of the two distributions are also significantly different. As expected,

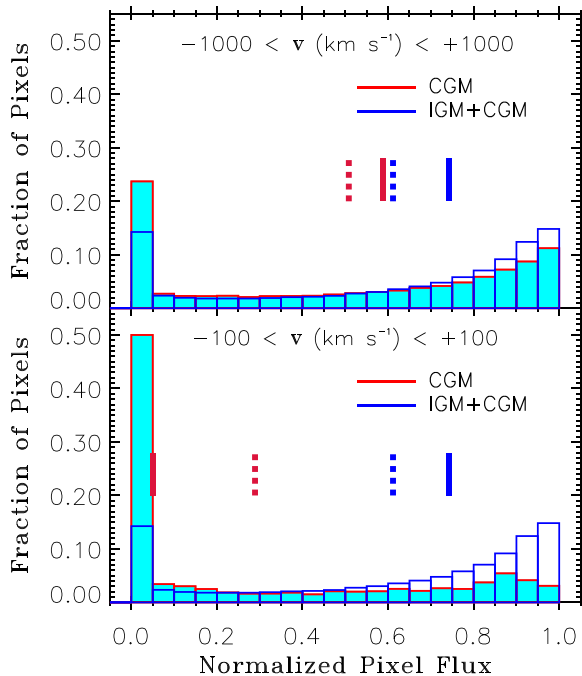


**Figure 5.** Histograms of Ly $\alpha$  pixel flux, labelled as CGM, within  $\pm 100$  km s $^{-1}$  (bottom) or  $\pm 1000$  km s $^{-1}$  (top) of the LAE redshift  $z_{\text{corr}}$  are compared with the histogram of pixel flux in the Ly $\alpha$ -forest regions of all the eight quasars (labelled as IGM + CGM). The median and mean values are indicated, respectively, by the solid and dashed vertical lines with corresponding colours. The distributions for the CGM are right-skewed showing a sharp peak in the lowest flux bin. The Ly $\alpha$ -forest flux distribution (IGM + CGM) shows the exact opposite trend. A two-sided KS-test suggest that the pixel flux distribution for the CGM is significantly different compared to that of the Ly $\alpha$ -forest. As expected, the difference is somewhat reduced in the top panel in which a 10 times larger velocity window around each  $z_{\text{corr}}$  is used.

the difference between the CGM and the Ly $\alpha$  forest pixel flux distributions is somewhat reduced ( $D_{\text{KS}} = 0.13$  and  $P_{\text{KS}} = 10^{-10}$ ) for the  $\pm 1000$  km s $^{-1}$  velocity window shown in the top panel. The mean (0.51) and median (0.59) values of the CGM pixel flux distribution for the  $\pm 1000$  km s $^{-1}$  velocity window are somewhat closer to the corresponding values for the Ly $\alpha$  forest pixel flux distribution. In the next section we show the CGM absorption as a function of LOS velocity, and indeed confirm that significant excess absorption is seen around galaxy redshifts.

#### 4.2 Flux and optical depth profiles for the full sample

The mean and median stacked absorption profiles of H I and C IV for the full sample are shown in the left-hand and middle panels of Fig. 6, respectively. For a given species (H I or C IV), the stacked absorption profile is generated by shifting the quasar spectra to the rest frame of each LAE using the  $z_{\text{corr}}$  values, and subsequently calculating the mean/median fluxes in bins of 50 km s $^{-1}$ . We verified that our results are insensitive to the bin size. However, we preferred a bin size of 50 km s $^{-1}$  in order to minimize the effects of correlated noise. Note that each quasar–galaxy pair provides an independent probe of the CGM. Thus, all quasar spectra were treated equally without putting any weight based on the  $S/N$  of the spectra around the wavelength ranges of interests. Since the typical  $S/N$  of the spectra is  $\gtrsim 30$  in the Ly $\alpha$  forest and  $\gtrsim 60$  redward of the QSO’s Ly $\alpha$  emission, the scatter in the stacked spectra is likely dominated by the stochastic nature of

the gaseous environments around galaxies, and not by the  $S/N$  of the individual spectra.

We would like to point out two features seen in the Ly $\alpha$  stacks shown in the left bottom and middle bottom panels of Fig. 6: (i) The effective continua (i.e. the pseudo-continua) determined at large velocities ( $> 3000$  km s $^{-1}$ ) from the line centre are considerably lower than the actual continuum level where the normalized flux is 1.0. This is due to the stochastic absorption in the Ly $\alpha$  forest. Indeed, the pseudo-continua levels for the mean (0.60) and median (0.72) stacks are very similar to the mean and median values we obtained for the Ly $\alpha$  forest pixel flux distribution (IGM + CGM) in the previous section (see §4.1). (ii) The median stacked Ly $\alpha$  absorption is significantly stronger than the mean stacked absorption. This is owing to the fact that the CGM pixel flux distribution is strongly right-skewed with median value much lower than the mean (see lower panel of Fig. 5). The pseudo-continuum for the median stacked profile is, however, somewhat higher compared to the mean stacked profile. Consequently, the Ly $\alpha$  rest-frame equivalent width ( $W_r$ ) measured for the median profile is considerably higher than that of the mean absorption profile as indicated in the figure.

The mean C IV absorption (top left panel in Fig. 6), on the contrary, is significantly stronger than the median C IV absorption (top middle panel), because the C IV pixel flux distribution is left-skewed. The pseudo-continuum for the median stack is higher compared to the mean stack. This is consistent with what is seen for Ly $\alpha$ , however, the pseudo-continua values are significantly higher for C IV compared to H I. This is expected since C IV falls in the red part of the quasar spectra where the line density for unrelated absorption is significantly lower than in the Ly $\alpha$  forest.

The 68 percent confidence intervals (Fig. 6) and standard deviations (not shown) of the stacked spectra are calculated from 1000 bootstrap realizations of the LAE sample. However, we do not use these asymmetric 68 percent confidence intervals in any measurements. Instead, we use the standard deviation of flux to obtain the errors on line centroid ( $V_0$ ) and line width ( $\sigma_v$ ) by fitting a single-component Gaussian to each stacked absorption profile. We do not use the bootstrap realizations of the stacks to derive uncertainties on  $V_0$  and  $\sigma_v$ , since the Gaussian fits did not converge for many realizations, particularly for the subsamples.

The line centroids of the mean and median stacked Ly $\alpha$  profiles are  $-8 \pm 11$  and  $-2 \pm 10$  km s $^{-1}$ , respectively, which are fully consistent with the systemic velocity (i.e. 0 km s $^{-1}$ ). Thus, the use of  $z_{\text{corr}}$ , instead of  $z_{\text{peak}}$ , naturally produces stacked profiles with line centroids consistent with the systemic velocity. This, however, is not true for every subsample that we explore here. In some cases, particularly for the weaker C IV stacks, we do notice residual offsets owing to sample variance and/or the large intrinsic scatter in the empirical relation used to correct the  $z_{\text{peak}}$  values. In passing, we note that the uncertainties in the line centroids (and  $\sigma_v$ ) we quoted here should be treated as lower limits, since the fitting errors do not take into account the fact that the noise in nearby spectral pixels is correlated for the adopted bin size of 50 km s $^{-1}$ .

The rest-frame equivalent width,  $W_r$ , for each absorption stack is derived from direct integration of the observed profiles within  $\pm 300$  km s $^{-1}$  (and  $\pm 500$  km s $^{-1}$ ) of the line centroid. Such velocity windows encompass most of the absorption (see Fig. 6), and are commonly used in the literature (e.g. Rudie et al. 2012; Werk et al. 2013). The uncertainties in the equivalent widths are determined from the stacks of the 1000 bootstrap samples. Finally, we calculated column densities using the  $W_r$  measured from the mean stacked profiles assuming that the line falls on the linear part of the curve of growth. We caution that the column densities quoted for H I

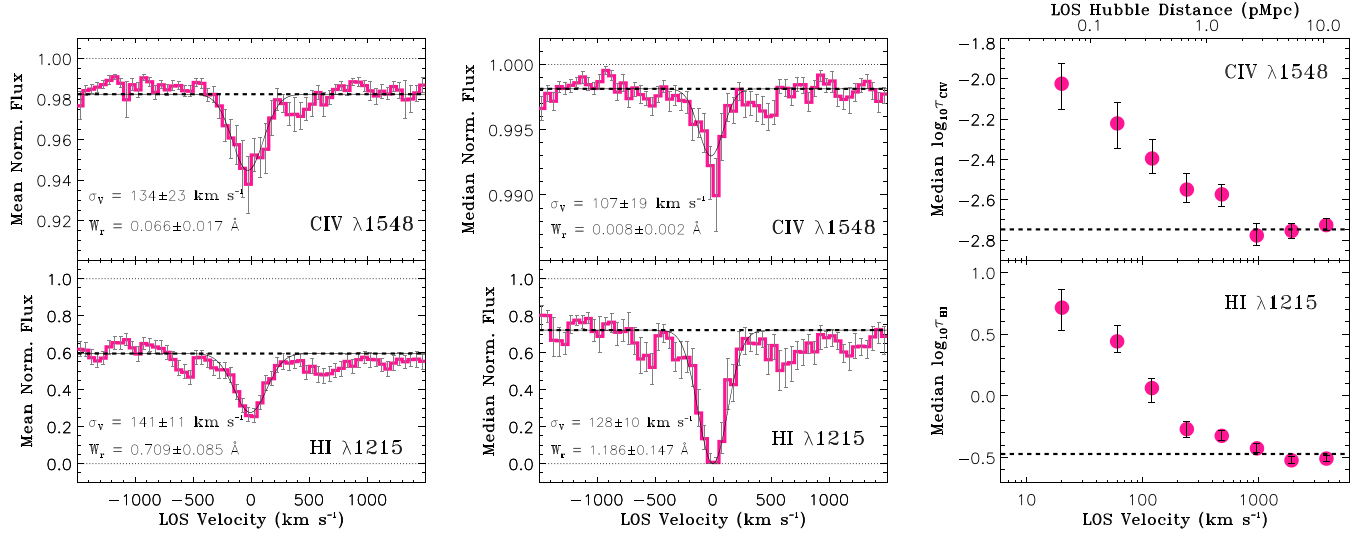


**Figure 6.** Left: Mean stacked absorption profiles of H I (bottom) and C IV (top) for the full sample of LAEs. Note the different y-axis ranges for H I and C IV. There are 77 (92) LAEs contributing to the H I (C IV) stack. The dotted lines at normalized flux value of 1.0 indicate the actual continua. The dashed lines show the pseudo-continua (i.e. the mean fluxes in random regions) for the stacked profiles, estimated far away from the systemic velocity. The 68 per cent confidence intervals in all panels are obtained from 1000 bootstrap realizations of the LAE sample. The best-fitting single-component Gaussian profiles are shown by the smooth black curves. The line widths, obtained from Gaussian fitting, and  $W_r$ , determined directly from the stacked profiles (within  $\pm 300$  km s<sup>-1</sup> of the line centroid), are indicated in the corresponding panels. The errors in  $W_r$  are estimated from the stacks of the bootstrap samples. Middle: The same as the left-hand panels but for median stacked absorption profiles. Right: Median stacked optical depth profiles of H I (bottom) and C IV (top) as a function of the absolute LOS velocity difference. The dashed lines indicate the median optical depth in random regions i.e. far away from the systemic velocity. The top axis indicates the proper LOS distance at  $z = 3.3$  (the median redshift) corresponding to the velocity plotted along the bottom axis, assuming pure Hubble flow.

stacks should be considered conservative lower limits, since the Ly  $\alpha$  stacks are heavily saturated. Tables A1 and A2 summarize all the measurements performed on the H I and C IV profiles, respectively, for all the stacks generated for this study.

The measured Ly  $\alpha$  equivalent width for the median stack of  $1.186 \pm 0.147$  Å ( $0.709 \pm 0.085$  Å for the mean stack) indicates that the line is heavily saturated, and detected at a  $>8\sigma$  significance. The  $W_r$  of  $0.008 \pm 0.002$  Å for C IV ( $0.066 \pm 0.017$  Å for the mean stack), on the other hand, suggests that the line is very weak but detected at a  $\approx 4\sigma$  significance. As mentioned earlier, C IV is the only metal line that is detected at a  $>3\sigma$  significance. The widths (i.e. velocity dispersions) of the H I and C IV profiles of  $128 \pm 10$  km s<sup>-1</sup> ( $141 \pm 11$  km s<sup>-1</sup> for the mean stack) and  $107 \pm 19$  km s<sup>-1</sup> ( $134 \pm 23$  km s<sup>-1</sup> for the mean stack), respectively, are consistent with each other. These line widths are much larger than expected from thermal broadening of  $\approx 10^4$  K gas.<sup>5</sup> The observed line width can be approximated as  $\sigma_v^2 = \sigma_{\text{int}}^2 + \sigma_{\text{eff}}^2$ , where  $\sigma_{\text{int}}$  is the intrinsic line width and  $\sigma_{\text{eff}}$  is the effective spectral resolution. The  $\sigma_{\text{eff}}$  will be dominated by the scatter in the relation used to obtain  $z_{\text{corr}}$ , and, to a lesser extent, by the bin size used (50 km s<sup>-1</sup>). The  $\sigma_{\text{int}}$  will have contributions from gravitational motions, dynamical processes such as inflow/outflow, and the Hubble flow.

The median optical depth profiles of H I and C IV are shown in the right-hand panel of Fig. 6. Instead of using the flux, here we used the optical depths for stacking. The median optical depth values are calculated in constant logarithmic LOS velocity bins of 0.301 dex. In order to increase the S/N, the optical depth profiles are made one-sided by using the absolute of LOS velocity difference. The errors in the optical depths (68 per cent confidence intervals) are calculated

<sup>5</sup>The thermal line widths ( $\sigma$ ) corresponding to a gas temperature of  $10^4$  K is only 9.1 and 2.6 km s<sup>-1</sup> for H I and C IV, respectively.

from 1000 bootstrap realizations of the LAE sample. The optical depth signals for both H I and C IV are significantly enhanced for LOS velocities  $\leq 500$  km s<sup>-1</sup>, compared to the values expected in random regions in the universe as indicated by the dashed horizontal lines in the plot. For LOS velocities  $\leq 30$  km s<sup>-1</sup>, the optical depths for both H I and C IV are enhanced by almost an order of magnitude. Owing to the large dynamic range of optical depth, such profiles are particularly useful to compare stacks constructed using different samples of galaxies.

### 4.3 Environmental dependence

The properties of the CGM of a galaxy may vary with the large-scale environment in which it resides. To examine the effects of the environment on the CGM absorption, we divided our sample into ‘isolated’ and ‘group’ subsamples. A galaxy (LAE) is called isolated if there is one and only one LAE detected within the MUSE FoV and within a linking velocity,  $v_{\text{link}}$ , of  $\pm 500$  km s<sup>-1</sup> of its redshift (‘all\_environment\_iso’ in Table 3). A total of 66/96 LAEs satisfy these criteria. For the remaining 30 ‘group’ LAEs, there is at least one companion LAE with an LOS velocity less than  $v_{\text{link}}$  (‘all\_environment\_group’ in Table 3). We emphasize here that by ‘group’ we *do not* necessarily refer to a virialized structure. It is rather a measure of overdensity. Fig. 7 shows the distribution of the number of LAEs in the ‘group’ subsample. There are a total of 10 ‘groups’, 60 per cent (20 per cent) of them consist of two (three) member LAEs, and 20 per cent of them have five or more LAEs. Note that we found 96 LAEs over a total redshift path length of  $\approx 6.8$ , leading to  $dN_{\text{LAE}}/dz$  of  $\approx 14$  and  $dN_{\text{LAE}}/dv$  of  $\approx 0.2$  for  $\delta v = 1000$  km s<sup>-1</sup>. Thus, detecting two LAEs within  $\pm 500$  km s<sup>-1</sup> corresponds to an overdensity of  $\approx 10$ .

The left-hand panels of Fig. 8 shows the mean stacked H I (bottom) and C IV (top) absorption profiles arising from the isolated (blue)

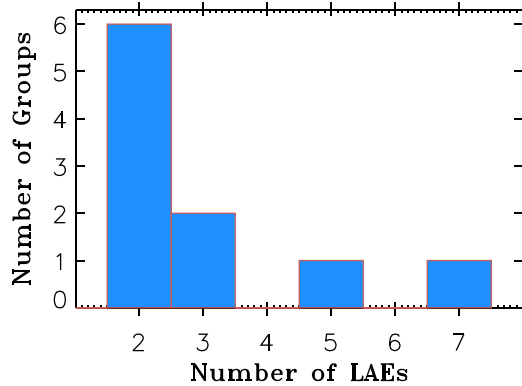


**Figure 7.** Histogram of the number of galaxies per group in the ‘group’ subsample. Most of the ‘groups’ in our sample consist of two detected LAEs.

and ‘group’ (red) subsamples. The corresponding median stacked profiles are shown in the right-hand panels. A strong environmental dependence, particularly for H I, is evident. The CGM absorption is significantly stronger for the ‘group’ galaxies compared to the isolated ones. The rest equivalent width measured from the mean H I profile, within a  $\pm 500 \text{ km s}^{-1}$  velocity window, for the ‘group’ galaxies is  $2.279 \pm 0.305 \text{ \AA}$  ( $1.467 \pm 0.210 \text{ \AA}$  for the mean stack), which is  $\approx 2.5$  times larger than that measured for the isolated galaxies (see Table A1). In addition, the width of the H I absorption is  $235 \pm 22 \text{ km s}^{-1}$  ( $241 \pm 24 \text{ km s}^{-1}$  for the mean stack) for the ‘group’ subsample which is  $\approx 2.8$  times larger than for the isolated subsample. The equivalent widths of both the median and mean stacked C IV profiles for the ‘group’ galaxies are somewhat larger than for the isolated galaxies (see Table A2). However, owing to the intrinsic weakness of the C IV profiles, the difference in equivalent width is only marginally significant.

The differences in strengths and widths of the H I absorption for the two subsamples are also evident from the optical depth profiles shown in the bottom panel of Fig. 9. The optical depths for the ‘group’ subsample (red star symbols) are consistently higher compared to the isolated subsample (blue filled circles) out to  $\approx 500 \text{ km s}^{-1}$ . The optical depth profile for the isolated subsample shows a sharp decline at LOS velocity of  $\approx 100 \text{ km s}^{-1}$ , and quickly become consistent with the value measured at random regions (dashed line). The decline in the ‘group’ optical depth profile, on the contrary, is more gradual with an excess optical depth seen out to  $\approx 500 \text{ km s}^{-1}$ . The difference in C IV absorption is also conspicuous as shown in the top panel, at least at small LOS velocities.

In order to investigate whether the observed strong environmental dependence is driven by any underlying properties of the LAEs in our sample, we performed several two-sided KS-tests. The median values of different properties of the isolated and ‘group’ subsamples and the KS-test results are summarized in Table 4. The distributions of these properties are not statistically different between the isolated and ‘group’ subsamples. Although the difference is not statistically significant, the median impact parameter of the isolated subsample is somewhat smaller compared to the ‘group’ subsample. However, this difference would produce the opposite effect (i.e. stronger CGM absorption for the isolated subsample) than what we find here. Besides, the median impact parameter of the closest (to the background quasar) members of the ‘group’ galaxies is  $152 \text{ pkpc}$ , which is very similar to the isolated subsample (Table 4). A two-sided KS-test is consistent with the hypothesis that the two distributions are drawn from the same parent populations ( $D_{KS} = 0.16$ ,  $P_{KS} = 0.97$ ). We therefore rule out the possibility that the observed difference is

driven by differences in the impact parameter distributions between the isolated and ‘group’ subsamples.

Owing to the limited FoV of MUSE, it is not possible to determine if an isolated galaxy at the edge of the field is truly isolated, since there might be companion LAEs just outside the FoV. If at all, this would produce stronger absorption for the isolated sample. However, we verified that the H I absorption for the isolated subsample does not change appreciably even if we exclude the LAEs at the edge of the FoV by selecting the isolated LAEs with  $\rho < 200 \text{ pkpc}$  only. Next, we used all 23/30 (30/30) ‘group’ LAEs satisfying our redshift bounds (see Table 3) for H I (C IV) stacking. We find that the environmental dependence remains significant even if we use only one LAE from each ‘group’ for stacking.<sup>6</sup> Finally, we find that the stronger absorption for the ‘group’ subsample is not entirely driven by the two ‘groups’ with the highest numbers of LAEs (see Fig. 7). The difference remains significant when we exclude the 12 LAEs (5 + 7) arising from the two ‘groups’. We therefore conclude that the observed environmental dependence of the CGM absorption is real and robust. It is quite remarkable that such a simple indicator of environment produces such a strong difference in H I absorption.

For the results presented above, we assumed a  $v_{\text{link}}$  of  $\pm 500 \text{ km s}^{-1}$  for defining the isolated/‘group’ galaxies. We verified that the strong environmental dependence persists for  $v_{\text{link}} = \pm 250 \text{ km s}^{-1}$ . However, the difference is reduced significantly for  $v_{\text{link}} = \pm 1000 \text{ km s}^{-1}$ . A velocity difference of  $1000 \text{ km s}^{-1}$  at  $z \approx 3.3$  corresponds to a length-scale of  $\approx 2.8 \text{ pMpc}$  assuming a pure Hubble flow. This length-scale is considerably larger than the scale of a typical galaxy group at similar redshifts. Therefore, the ‘group’ subsample defined with  $v_{\text{link}} = 1000 \text{ km s}^{-1}$  includes LAEs that are isolated (i.e. not related dynamically). Consequently, the CGM absorption of the corresponding ‘group’ sample is weakened, suppressing the strong environmental dependence otherwise seen for smaller  $v_{\text{link}}$  values.

Besides being wider and stronger, the Ly $\alpha$  stack for the ‘group’ subsample seems to show marginally significant secondary peaks both blue- ( $\approx [-900, -400] \text{ km s}^{-1}$ ) and red- ( $\approx [+500, +1000] \text{ km s}^{-1}$ ) ward of the primary peak at  $\approx 0 \text{ km s}^{-1}$  (Fig. 8). Peaks at particular velocities other than zero are not expected a priori. Indeed, the peaks at negative and positive velocities appear at somewhat different absolute velocity separations. A measurement of their true significance would thus have to account for the ‘look elsewhere effect’, i.e. the fact that it is more likely to find a noise spike somewhere when we search over a larger velocity interval, as well as for the correlations between neighbouring pixels. These corrections would further decrease the significance of the secondary peaks. Such an analysis is best done using comparisons with forward models with mock/simulation data, which is beyond the scope of this study and in our opinion unwarranted given the already marginal significance of the enhancement of the optical depth compared to random regions (Fig. 9).

#### 4.4 Impact parameter dependence

Determining how gas and metals are distributed around our galaxies is one of our primary goals. We thus generated stacks of H I and C IV lines for the three different impact parameter bins (‘all- $\rho_{\text{low}}$ ’, ‘all- $\rho_{\text{mid}}$ ’, and ‘all- $\rho_{\text{high}}$ ’ in Table 3) corresponding to the three tertiles of the  $\rho$ -distribution. Since a strong environmental dependence was seen in the previous section, we further generated

<sup>6</sup>Eight (ten) galaxies from the 10 ‘groups’ satisfy the redshift bounds for the H I (C IV) stacking.

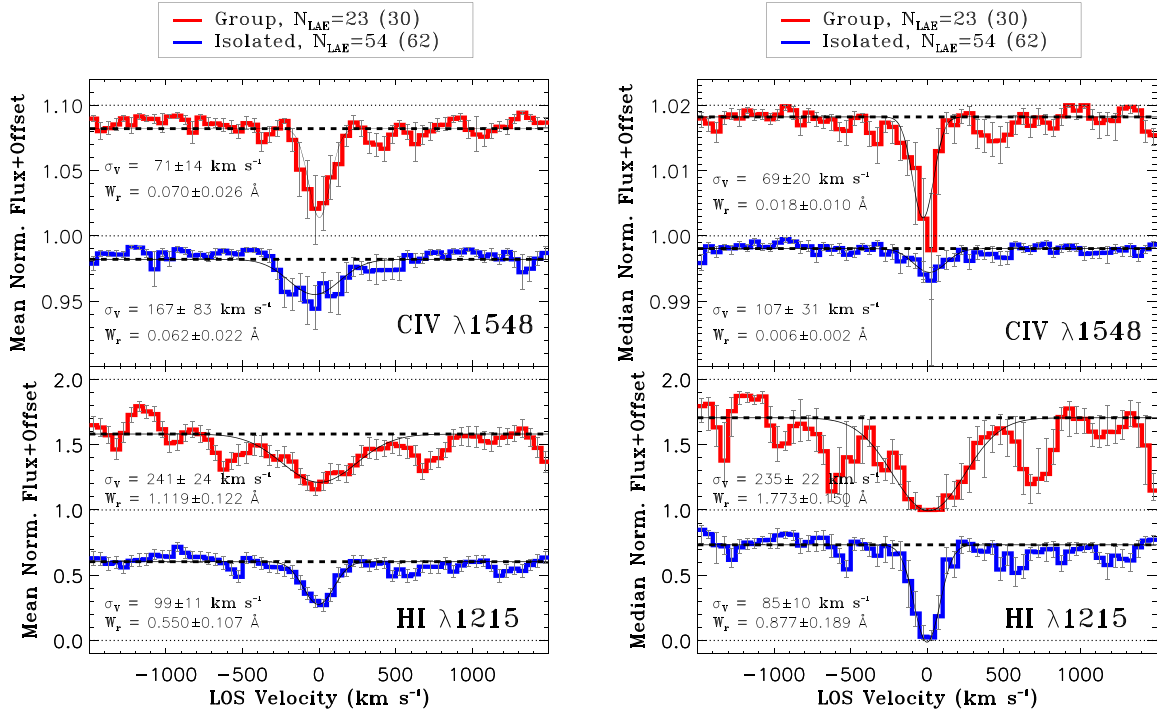


**Figure 8.** Left: Mean stacked H I (bottom) and C IV (top) profiles for the isolated and ‘group’ subsamples as marked by the legends on the top. The number of LAEs contributing to the H I stack is indicated. The corresponding number for the C IV stack is given in parentheses. The stacked profiles for the ‘group’ subsample are shifted vertically by 1.0 for H I and by 0.10 for C IV for clarity. All other features are the same as described in Fig. 6. Right: The same as the left-hand panels but for median stacked profiles. The C IV profile for the ‘group’ subsample is offset by 0.02 for clarity. A strong (marginal) environmental dependence is seen for the Ly  $\alpha$  (C IV) absorption.

stacks for three impact parameter bins (‘iso- $\rho$ \_low’, ‘iso- $\rho$ \_mid’, and ‘iso- $\rho$ \_high’ in Table 3) using only the isolated LAEs (‘isolated only’).

The median optical depth profiles of H I and C IV for the three impact parameter bins constructed from the full sample are shown in the left-hand panel of Fig. 10. The right-hand panel of the figure shows the corresponding profiles for the isolated LAEs. Owing to the smaller sample sizes, the profiles in the right-hand panel are noisier. We do not find any significant impact parameter dependence of H I or C IV absorption. The optical depth profiles are consistent with each other within the allowed uncertainties across the whole LOS velocity range.

While the profiles of absorption as a function of LOS velocity are important, redshift space distortions due to peculiar motions complicate their interpretation. The dependence of the  $W_r$  and column density of different species (neutral hydrogen and metal ions) on impact parameter provides complementary information on the overall distribution of circumgalactic gas and metals. Fig. 11 shows the median equivalent widths of H I and C IV absorption as a function of impact parameter. The corresponding flux profiles are shown in Figs S1 and S2. The H I and C IV equivalent widths measured from these profiles are summarized in Tables A1 and A2, respectively. Interestingly, the H I  $W_r$ -profile for the full sample (open red circles) is flat with a slope  $dW_r/d\rho \approx 0$ . This is true for both the median and mean (not shown) stacked profiles. The H I  $W_r$ -profiles corresponding to the ‘isolated only’ sample (filled blue circles) are noisier owing to the smaller sample sizes. However, no significant trend with impact parameter is seen even for the ‘isolated only’ sample either. We note here that for galaxies near the edge of the FoV we can only search for neighbours on one side, whereas

for galaxies in the centre we can search for group members on all sides. This may lead us to misclassify group galaxies near the edge of the field as isolated objects. Because the absorption is stronger around group galaxies, this ‘edge effect’ may bias us to overestimate the absorption for larger impact parameters for the ‘isolated only’ sample, thus obscuring a possible trend of decreasing absorption with increasing galactocentric distance.

Due to the intrinsic weakness of the C IV absorption, the corresponding  $W_r$ -profiles are significantly more noisier. Given the large uncertainties in individual measurements, we cannot draw any robust conclusion on the C IV  $W_r$ -profile. However, a tentative negative trend is seen between C IV equivalent width and impact parameter when we split the ‘isolated only’ sample into two  $\rho$  bins.

#### 4.5 Redshift dependence

The LAEs in our sample span the redshift range 2.92–3.82, covering  $\approx 0.6$  Gyr of cosmic time. In this section, we inspect whether there is any redshift evolution of the CGM absorption. Note that the redshift range probed by our sample is too small to expect strong evolution. For this exercise, we first exclude the 30 ‘group’ LAEs in order to eliminate any possible effects due to the environment. The remaining 66 LAEs are divided into two subsamples iso- $z_{\text{peak}}$ \_low and iso- $z_{\text{peak}}$ \_high (see Table 3 for details) bifurcated at the median redshift.

The optical depth profiles of H I and C IV corresponding to these two subsamples are shown in Fig. 12. They do not show any dependence on redshift. The rest-frame equivalent widths measured from the stacked profiles (see Fig. S3) also confirm the lack of any

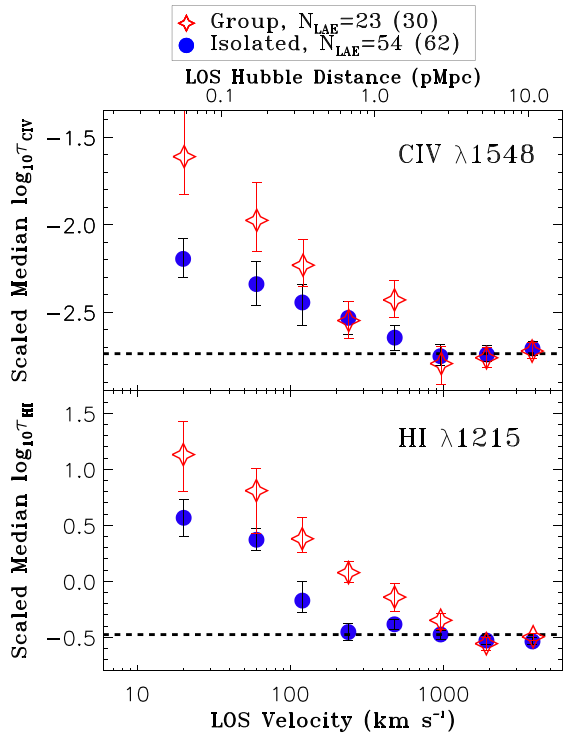


**Figure 9.** The median optical depth profiles of H I (bottom) and C IV (top) for the isolated (blue filled circles) and ‘group’ (red star symbols) subsamples. The top axis indicates the proper LOS distance at  $z = 3.3$  corresponding to the velocity plotted along the bottom axis, assuming pure Hubble flow. To facilitate a proper comparison, the profiles of isolated and ‘group’ subsamples are taken to the same common baseline by linearly shifting one of the profiles by the difference in the background levels measured for the two profiles. A strong environmental dependence is seen for both H I and C IV with larger excess absorption around LAEs in ‘groups’.

**Table 4.** Statistics of the isolated and ‘group’ subsamples.

Properties (1)	Isolated (2)	Group (3)	KS-test results (4)
$\rho$ (pkpc)	153.1	194.7	$D = 0.22, P = 0.26$
$z$	3.35	3.32	$D = 0.21, P = 0.31$
$\log_{10} L(\text{Ly } \alpha) / \text{erg s}^{-1}$	41.99	41.97	$D = 0.10, P = 0.98$
FWHM ( $\text{km s}^{-1}$ )	248.9	231.6	$D = 0.14, P = 0.76$
$\log_{10} \text{SFR} / M_{\odot} \text{ yr}^{-1} \text{ }^a$	-0.13	-0.02	$D = 0.19, P = 0.44$
$EW_0$ ( $\text{\AA}$ ) <sup>a</sup>	48.3	52.3	$D = 0.22, P = 0.29$

*Notes.* (1) Properties; (2) Median value of the property in #1 for the isolated subsample; (3) Median value of the property in #1 for the ‘group’ subsample; (4) Results of the two-sided KS-test performed on the isolated and ‘group’ subsamples for the property in #1. Here,  $D$  denotes the maximum difference between the cumulative distributions, and  $P$  denotes the probability of obtaining the value  $D$  by chance. <sup>a</sup>Excluding the 15 LAEs blended with low- $z$  continuum emitters and assuming limits for the continuum undetected LAEs as measurements.

significant redshift evolution in the CGM absorption in our sample (see Tables A1 and A2).

#### 4.6 Ly $\alpha$ luminosity dependence

Next, we investigate the dependence of CGM absorption on the Ly  $\alpha$  line luminosity,  $L(\text{Ly } \alpha)$ . In order to avoid any underlying

environmental dependence as seen in Section 4.3, we will use only the isolated LAEs for this analysis. The  $L(\text{Ly } \alpha)$  of the isolated LAEs span the range of  $10^{41.3} - 10^{42.9} \text{ erg s}^{-1}$ , with a median value of  $10^{42.0} \text{ erg s}^{-1}$ . To investigate the  $L(\text{Ly } \alpha)$  dependence, we split the isolated LAEs into two subsamples (‘iso- $L(\text{Ly } \alpha)$ .low’ and ‘iso- $L(\text{Ly } \alpha)$ .high’) about the median value (see Table 3 for details).

The optical depth profiles of H I and C IV for these two subsamples are shown in Fig. 13. Neither shows any trend with  $L(\text{Ly } \alpha)$ . The flux profiles, shown in Fig. S4, also confirm the lack of any strong  $L(\text{Ly } \alpha)$  dependence. None the less, we note that the equivalent widths of both H I and C IV are somewhat higher for the iso- $L(\text{Ly } \alpha)$ .high subsample compared to the iso- $L(\text{Ly } \alpha)$ .low subsample, but consistent with each other within the  $1\sigma$  allowed ranges (see Tables A1 and A2). We point out that the median  $L(\text{Ly } \alpha)$  of the iso- $L(\text{Ly } \alpha)$ .high sample is only a factor  $\approx 3.3$  higher compared to the iso- $L(\text{Ly } \alpha)$ .low sample. Samples with larger dynamic ranges in  $L(\text{Ly } \alpha)$  are required to confirm this tentative trend.

#### 4.7 FWHM dependence

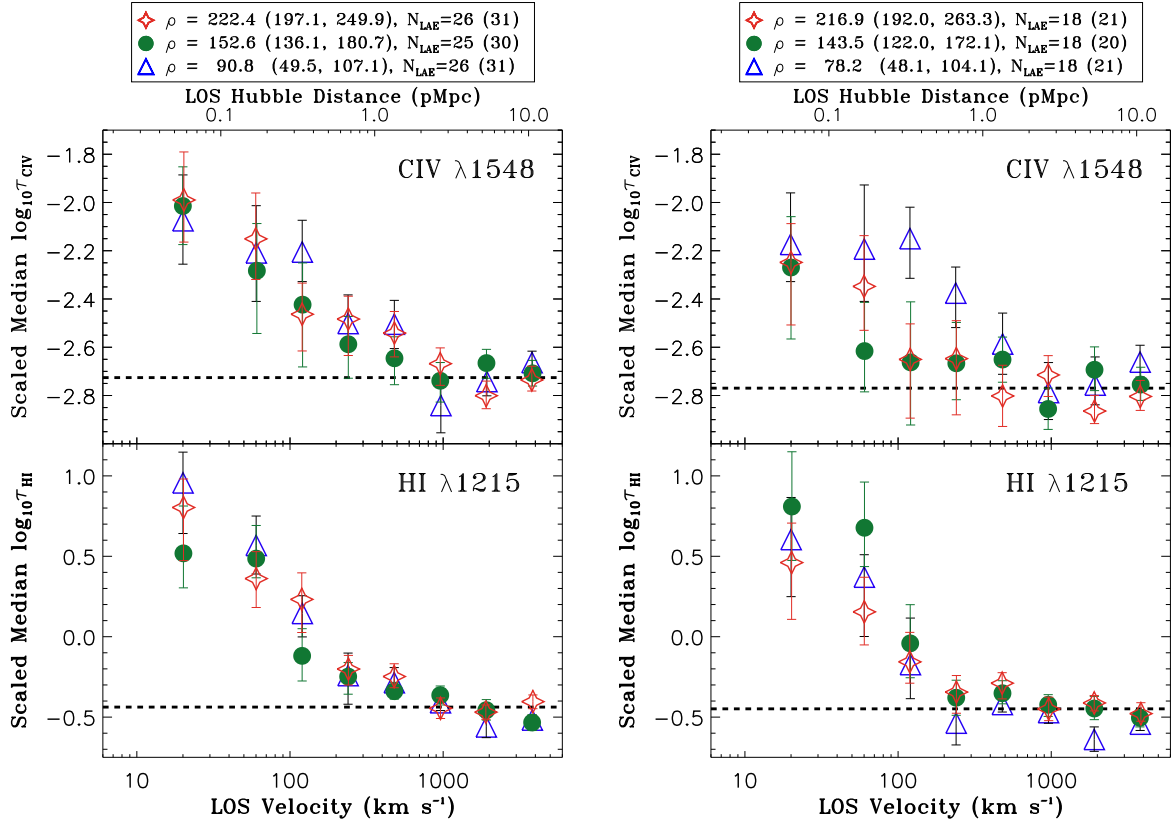
The FWHM of an emission line is expected to be correlated with its luminosity since both are related to the area under the line. We found a strong ( $4.4\sigma$ ) correlation between  $L(\text{Ly } \alpha)$  and FWHM in our sample (see Fig. 4). None the less, there is a significant scatter in the relation. We thus investigate here whether the CGM absorption depends on the FWHM of the Ly  $\alpha$  emission line. Note that, the FWHM of the Ly  $\alpha$  lines were directly calculated from the MUSE spectra without any modelling and without correcting for the instrumental broadening. The median FWHM of the 66 isolated LAEs is  $248.9 \text{ km s}^{-1}$ . We generated two subsamples ‘iso-FWHM.low’ and ‘iso-FWHM.high’ by bifurcating the isolated LAEs at the median FWHM value. The median FWHM and 68 percentile ranges of each subsamples are summarized in Table 3.

Fig. 14 shows the stacked H I and C IV optical depth profiles for the two FWHM bins. Both the H I and C IV optical depth measurements for the two bins are consistent with each other within the  $1\sigma$  uncertainties, suggesting a lack of a strong FWHM dependence. The equivalent widths measured from the flux profiles (see Fig. S5) for the two FWHM bins are also consistent with each other (see Tables A1 and A2). We, however, note that the H I line widths measured for the iso-FWHM.low sample is somewhat larger than that of the iso-FWHM.high sample. This is likely due to the larger scatter in the FWHM distribution for the iso-FWHM.low sample (Table 3) leading to larger redshift errors. Recall that we used the empirical FWHM- $V_{\text{offset}}$  relation to correct the Ly  $\alpha$  redshifts.

According to models of Ly  $\alpha$  radiative transfer (e.g. Verhamme et al. 2015), the FWHM of Ly  $\alpha$  emission is expected to correlate with the neutral hydrogen column density ( $N(\text{H I})$ ) of a galaxy. Thus, the absence of FWHM dependence may suggest a lack of strong trend between the H I content of galaxies and the neutral gas in their environments.

#### 4.8 SFR dependence

Star formation-driven large-scale winds are ubiquitous in high-redshift galaxies. The SFR is thus thought to be one of the key parameters that shapes the distributions of gas and metals surrounding galaxies. The dust-uncorrected SFRs of the LAEs in our sample are estimated from the UV continuum luminosity. Out of the 77 (92) LAEs satisfying the redshift limits for the H I (C IV) stack, 30 (38) are detected in the UV continuum emission. 17/30 (18/38 for C IV) LAEs are from the isolated subsample. Because of the small



**Figure 10.** Left: Similar to Fig. 9 but for the three impact parameter bins: all\_ρ\_low, all\_ρ\_mid, all\_ρ\_high, as defined in Table 3. The median values and 68 percentile ranges in the parentheses in the legends are for the LAEs contributing to the H I stack. The corresponding values for the C IV stack can be found in Table 3. Right: The same as the left-hand panels but for the iso\_ρ\_low, iso\_ρ\_mid, and iso\_ρ\_high subsamples (see Table 3). Neither H I nor C IV absorption show any significant, systematic dependence on impact parameter.

sample size, we used all 30 (38) UV-continuum-detected LAEs to investigate the SFR dependence of H I (C IV) absorption irrespective of their environments. The details of the two SFR bins (‘all\_SFR\_low’ and ‘all\_SFR\_high’) are given in Table 3. We created a third SFR bin (‘all\_SFR\_non-det’) containing all the UV-continuum-undetected objects.

The median stacked H I and C IV absorption spectra corresponding to the three subsamples are shown in Fig. 15 and the measurements performed on the stacked profiles are summarized in Tables A1 and A2. The median H I equivalent width ( $1.638 \pm 0.219 \text{ \AA}$ ) measured for the all\_SFR\_high bin is  $\approx 1.8$  times ( $\approx 1.6$  times for the mean stack) larger than that of the all\_SFR\_low bin. The difference is significant at the  $>3\sigma$  level. Besides being stronger, the H I absorption is  $\approx 2$  times wider ( $>3\sigma$ ) for the all\_SFR\_high bin with  $\sigma_v = 161 \pm 16 \text{ km s}^{-1}$  ( $154 \pm 19 \text{ km s}^{-1}$  for the mean stack) as compared to the all\_SFR\_low bin. The larger  $W_r$  and  $\sigma_v$  of the stacked H I profile for the all\_SFR\_high bin are also prominent in the optical depth profile shown in the bottom panel of Fig. 16. Therefore, we find that the circumgalactic Ly $\alpha$  absorption in our sample depends strongly on the SFR of the host LAEs. The detection significance for C IV is  $<3\sigma$  for all of the stacks (see top panel of Fig. 15). No obvious trend is seen from the noisy optical depth profiles shown in the top panel of Fig. 16.

Is the strong SFR dependence seen for H I driven by the environmental dependence we noticed in Section 4.3? We find that 7/15 LAEs contributing to the H I stack for the all\_SFR\_low subsample

are part of ‘groups’. For the all\_SFR\_high subsample, 6/15 of LAEs contributing to the H I stack are part of ‘groups’. Thus, the number of ‘group’ LAEs contributing to the two competing SFR bins are very similar. We also note here that, depending on the observed SFR, the member galaxies of a given ‘group’ will contribute to different SFR bins.<sup>7</sup> We thus believe that the observed trend with SFR cannot be fully attributed to the environmental dependence.

In order to investigate further, we generated H I stacks (not shown) using the 54 isolated galaxies (see Table 3). Only 17/54 are detected in UV continuum emission, allowing us to measure the SFRs (27 non-detections, 10 LAEs are blended with low- $z$  objects). No significant difference is seen in the stacked H I absorption spectra for the 13/17 UV-continuum-detected LAEs with  $\log \text{SFR}/M_\odot \text{ yr}^{-1} > -0.25$  (median  $\log \text{SFR}/M_\odot \text{ yr}^{-1} = 0.15$ ) and 15/27 UV-continuum-undetected LAEs with  $\log \text{SFR}/M_\odot \text{ yr}^{-1} < -0.25$ . The same is true for the C IV stack. However, we point out here that the median SFR of the 13 isolated LAEs in this exercise is lower than the median SFR of the all\_SFR\_high bin, and only 8 LAEs have  $\log \text{SFR}/M_\odot \text{ yr}^{-1} > 0.1$  whereas all the 15 LAEs in the all\_SFR\_high bin show  $\log \text{SFR}/M_\odot \text{ yr}^{-1} > 0.1$ . Thus the lack of trend with SFR for the isolated LAEs may owe to the smaller number

<sup>7</sup>For example, 5 of the member galaxies from the ‘group’ with the highest number (7) of galaxies (Fig. 7) are detected in the UV continuum. 2/5 LAEs contribute to the all\_SFR\_low bin, and the remaining 3 LAEs contribute to the all\_SFR\_high bin.

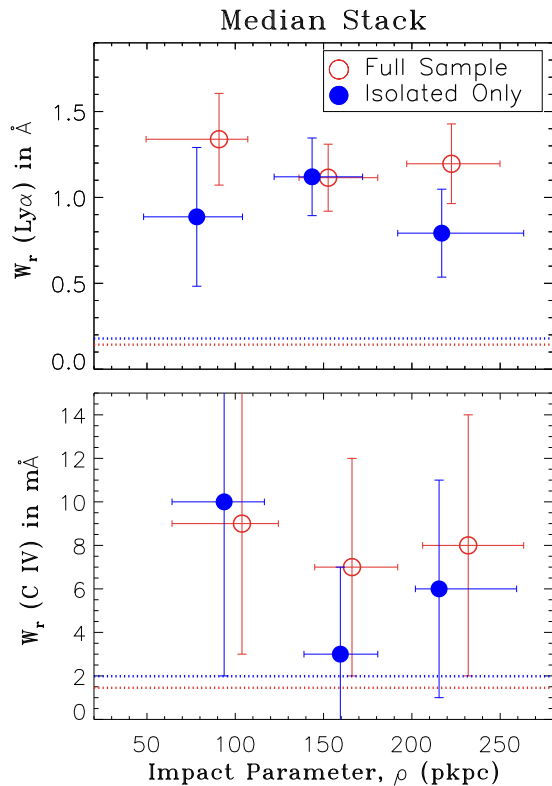


**Figure 11.** Rest equivalent widths measured within  $\pm 300 \text{ km s}^{-1}$  of the line centroids of the median stacked absorption profiles of Ly $\alpha$  (top) and C IV (bottom) as a function of impact parameter. The  $W_r$ -profiles for the full sample are shown by the open red circles, whereas the filled blue circles are for the ‘isolated only’ subsample. The error bars along the x-axis indicate 68 percentile ranges. The error bars along y-axis are the  $1\sigma$  measurement uncertainties from bootstrap resampling. The horizontal dotted lines represent the  $3\sigma$  limiting  $W_r$  values. The limiting  $W_r$  values are calculated from the continuum  $S/N$  of the stacked spectra and assuming a line width,  $\sigma_v$ , of  $100 \text{ km s}^{-1}$ . We do not find any significant trend between CGM absorption and  $\rho$  for the impact parameter range probed by our survey.

of isolated high-SFR LAEs reducing the dynamic range in SFR. Nevertheless, this does suggest the possibility that the trend seen in the full sample may be partly driven by the underlying environmental dependence.

The impact parameter distributions of the all\_SFR\_low and all\_SFR\_high subsamples are not statistically different ( $D_{KS} = 0.2$ ,  $P_{KS} = 0.90$ ), but the median  $\rho$  for the all\_SFR\_low sample (164.5 pkpc) is somewhat larger than that of the all\_SFR\_high sample (136.1 pkpc). This is unlikely to drive the observed SFR dependence since we do not find a significant trend between H I absorption and impact parameter (Section 4.4).

Finally, we point out that the widths and strengths of the mean and median Ly $\alpha$  absorption for the UV-continuum-undetected objects (all\_SFR\_non-det) are consistent with those of the all\_SFR\_low subsample. This is not surprising since the bulk of the SFR upper limits are similar to the SFRs measured for the all\_SFR\_low subsample.

#### 4.9 $EW_0$ dependence

The rest-frame equivalent width of Ly $\alpha$  emission ( $EW_0$ ) depends on both line and continuum fluxes ( $EW_0 = \text{line flux}/\text{continuum flux}$

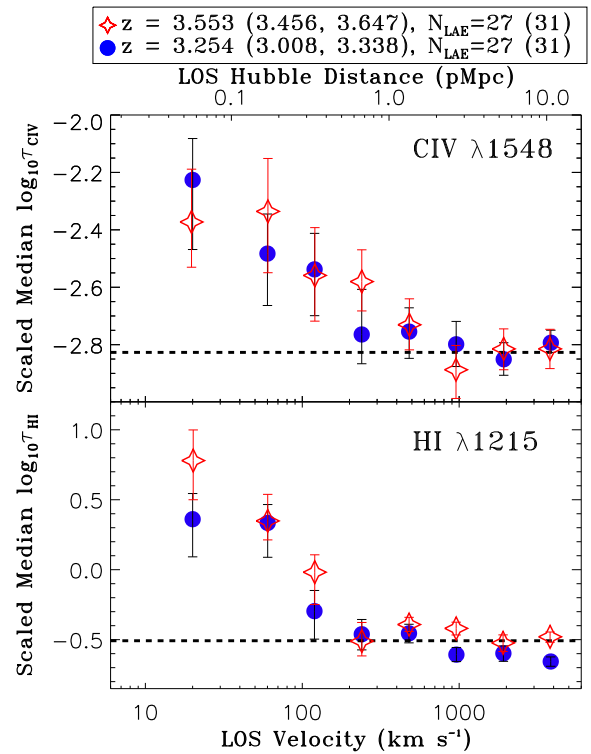


**Figure 12.** Similar to Fig. 9 but for two different redshift bins (iso- $z_{\text{peak\_low}}$  and iso- $z_{\text{peak\_high}}$ ). The median redshifts and 68 percentile ranges in the parentheses in the legends are for the LAEs contributing to the H I stack. The corresponding values for the C IV stack can be found in Table 3. No significant dependence on redshift is seen for either H I or C IV absorption.

density  $\propto L(\text{Ly}\alpha)/\text{SFR}$ ). We noticed a strong positive trend between H I absorption and SFR (Section 4.8), and only a marginal trend with  $L(\text{Ly}\alpha)$  (Section 4.6). Here, we investigate whether the CGM absorption shows any trend with  $EW_0$ .

Following the same strategy as in the previous section, we split the 30 (38 for C IV) UV-continuum-detected LAEs into all\_ $EW_0$ \_low and all\_ $EW_0$ \_high subsamples at the median  $EW_0$  of  $41.5 \text{ \AA}$  ( $48.7 \text{ \AA}$  for C IV) irrespective of their environments. The details for these two subsamples are given in Table 3. The stacked optical depth profiles corresponding to these two subsamples are shown in Fig. 17, and the measurements performed on the stacked flux profiles (see Fig. S6) are summarized in Tables A1 and A2. There is no significant difference in the optical depths of the two subsamples across the whole range of LOS velocities, suggesting a lack of a strong dependence on  $EW_0$  for both H I and C IV.

## 5 DISCUSSION

In this section, we discuss the main results of our survey in the context of other CGM surveys. The CGM surveys in the literature are for more massive galaxies and mostly at low- $z$ . Before we move on, we recall that the median halo (stellar) mass for our sample is estimated to be  $\sim 10^{11.1} M_{\odot}$  ( $\sim 10^{8.6} M_{\odot}$ ), which corresponds to a virial radius ( $R_{200}$ ) of only  $\approx 35 \text{ pkpc}$  (see section 5 of Muzahid et al. 2020). This suggests that they are Small Magellanic Cloud (SMC)-type objects. Almost all of the existing CGM surveys deal with galaxies that are significantly more massive (by an order of magnitude in stellar mass) than the objects in our sample.

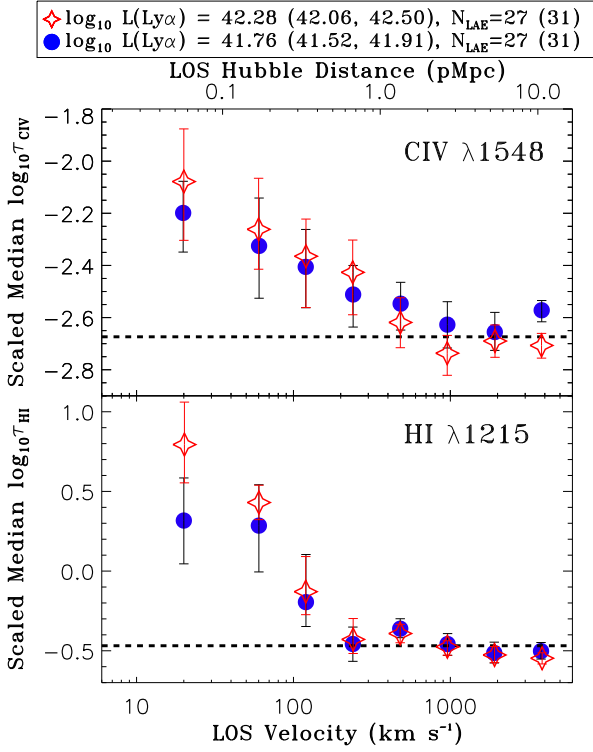


**Figure 13.** Similar to Fig. 9 but for two different luminosity bins ( $\text{iso}_L(\text{Ly}\alpha)_{\text{low}}$  and  $\text{iso}_L(\text{Ly}\alpha)_{\text{high}}$ ). The median luminosities and 68 percentile ranges in the parentheses in the legends are for the LAEs contributing to the H I stack. The corresponding values for the CIV stack can be found in Table 3. No significant dependence on  $\text{Ly}\alpha$  line luminosity is seen for either H I or CIV absorption.

### 5.1 Reservoirs of gas and metals around LAEs

We detected  $\text{Ly}\alpha$  and C IV  $\lambda 1548$  absorption in the composite spectra with  $\geq 4\sigma$  significance (Fig. 6). Given the median impact parameter (165 pkpc) and the median virial radius ( $\approx 35$  pkpc) of our sample, such detections reveal the presence of diffuse gas and metal reservoirs out to at least  $5R_{\text{vir}}$  surrounding the  $\text{Ly}\alpha$  emitting galaxies.

In Fig. 18, we compare the  $W_r$ -profile of H I  $\lambda 1215$  of our sample (red circles) with the ones from the literature. The blue squares represent observations from Steidel et al. (2010, see their table 4), who used stacking of background galaxy spectra to probe the CGM of 512 LBGs out to 125 pkpc. An extension of this study was recently presented by Chen et al. (2020) with 200 000 background-foreground galaxy pairs. The dashed line represents the empirical relation from Chen et al. (2020). The median halo mass of these LBGs is  $\approx 10^{12} M_{\odot}$ , corresponding to a virial radius of  $R_{200} \approx 90$  pkpc at the median redshift ( $z \approx 2.3$ ) of their sample. The median SFR of the LBG sample is  $\approx 25 M_{\odot} \text{ yr}^{-1}$ . Note that the median halo mass and SFR of the LBG sample are an order of magnitude higher than for our LAE sample. The green star symbols represent observations from Turner et al. (2014, see their table 8) who used background quasars to probe the CGM of  $z \approx 2.3$  LBGs drawn from the KBSS (Steidel et al. 2014), which is essentially the same set of LBGs presented in Steidel et al. (2010) but probed at larger impact parameters. The small triangles in Fig. 18 are from the COS-Halos (Tumlinson et al. 2013) and COS-GASS (Borthakur et al. 2015) surveys. Both these surveys characterize the CGM of  $\sim L_*$  galaxies at  $z < 0.4$  with stellar masses in the range  $M_* \sim 10^{9.5-11.5} M_{\odot}$ . The small orange diamonds

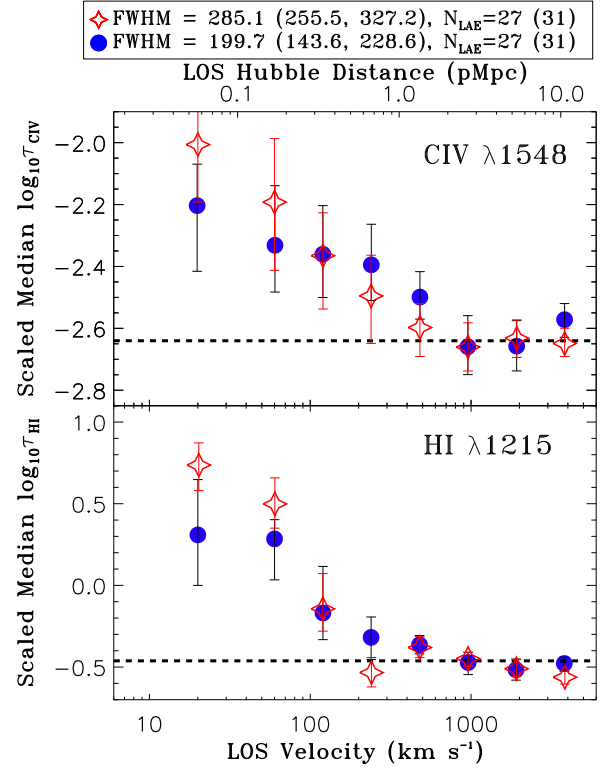


**Figure 14.** Similar to Fig. 9 but for two different FWHM bins ( $\text{iso}_{\text{FWHM}}_{\text{low}}$  and  $\text{iso}_{\text{FWHM}}_{\text{high}}$ ). The median FWHM values and 68 percentile ranges in the parentheses in the legends are for the LAEs contributing to the H I stack. The corresponding values for the CIV stack can be found in Table 3. No significant dependence on FWHM of  $\text{Ly}\alpha$  emission is seen for either H I or CIV absorption.

represent the measurements for sub- $L_*$  ( $0.1 < L/L_* < 1.0$ ) galaxies at  $z \approx 0.1$  from Prochaska et al. (2011, see their table 8). The small plus symbols are from the  $z \approx 0.15$  dwarf galaxy (median  $M_* \approx 10^{8.3} M_{\odot}$ ,  $L/L_* < 0.1$ ) sample of Johnson et al. (2017, see their table 1). For all three samples, the open symbols represent upper limits. The individual measurements for each sample are split into two impact parameter bins. The two big triangles, diamonds, and plus symbols represent the corresponding mean  $W_r$  at the median  $\rho$  of the two bins. The error bars on them are standard deviations. The censored data points (upper limits) are taken into account in calculating the mean  $W_r$  and standard deviations in each bins using survival analysis.<sup>8</sup>

The left-hand panel of Fig. 18 shows that the  $\text{Ly}\alpha$  equivalent widths measured for the LAEs in our sample are comparable to those measured for  $z \approx 2.3$  LBGs (Steidel et al. 2010; Turner et al. 2014; Chen et al. 2020) and  $\sim L_*$  galaxies at low- $z$  (Tumlinson et al. 2013; Borthakur et al. 2015). The  $W_r(\text{Ly}\alpha)$  for the low- $z$  sub- $L_*$  and dwarf galaxies are, however, considerably lower compared to our sample. In the right-hand panel of Fig. 18, we show the mean  $W_r(\text{Ly}\alpha)$  of the same samples as a function of normalized impact parameters,  $\rho/R_{200}$ . Such an  $x$ -axis minimizes the effects of different galaxy masses and redshifts for the different samples provided that the structure/properties of the CGM are self-similar. For the COS-Halos, COS-GASS, and the dwarf galaxy samples, the  $R_{200}$  values

<sup>8</sup>We used the ‘*cenken*’ function under the NADA package in R (<http://www.r-project.org/>).

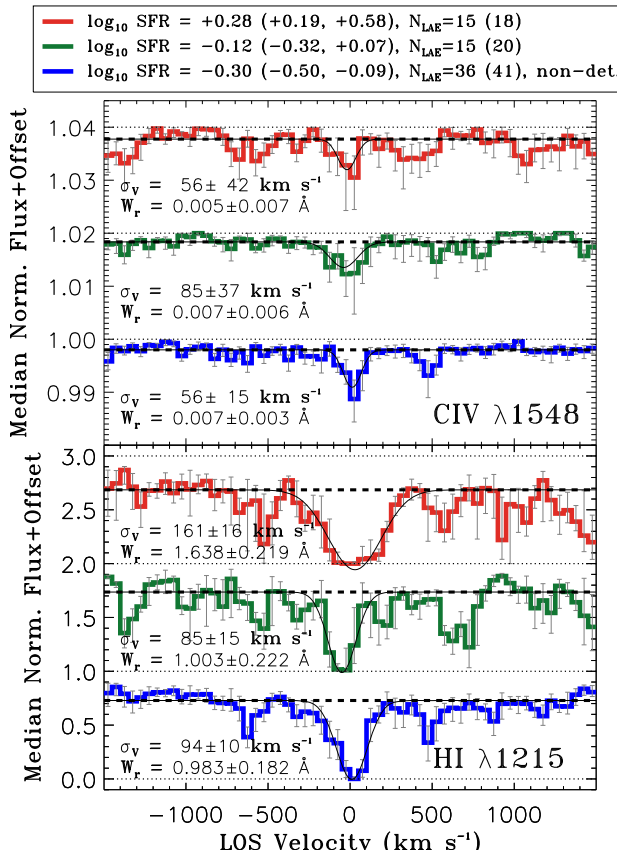


**Figure 15.** Similar to the right-hand panel of Fig. 8 but for three different SFR bins (all\_SFR\_non-det, blue; all\_SFR\_low, green; and all\_SFR\_high, red). The profiles in blue represent the subsample of the UV-continuum-undetected objects. The median SFR values and 68 percentile ranges in the parentheses in the legends are for the LAEs contributing to the H I stack. The corresponding values for CIV stack can be found in Table 3. The H I absorption shows a strong dependence on the SFR. The noisier CIV absorption profiles do not show any significant differences.

for the individual galaxies are available. For the sub- $L_*$  galaxies, we used the median  $R_{200} \approx 160$  pkpc as suggested by Prochaska et al. (2011). For the LBG samples we used  $R_{200} \approx 90$  pkpc (Turner et al. 2014). The right-hand panel of Fig. 18 conveys a couple of important messages: (1) For a fixed normalized impact parameter, the environment of  $z \approx 2.3$  LBGs is more enriched in H I compared to the dwarf ( $<0.1L_*$ ), sub- $L_*$  ( $<L_*$ ), and  $L_*$  galaxies at  $z \approx 0.2$ . (2) The environments of the LAEs in our sample are significantly more H I-rich compared to those of the LBGs at  $z \approx 2.3$  for a fixed normalized impact parameter.

A compilation of CIV  $W_r$ -profiles is shown in the left-hand panel of Fig. 19. The red circles represent our  $W_r$  measurements from the mean stacked spectra (open red circles are for the ‘isolated only’ subsample). The blue squares and green stars symbols are for the  $z \approx 2.3$  LBGs from Steidel et al. (2010, table 4) and Turner et al. (2014, table 8), respectively. The orange diamonds are for  $z \approx 2$  quasar host-galaxy sample of Prochaska et al. (2014, see their table 3).<sup>9</sup> The small magenta triangles indicate the measurements from the COS-dwarf survey ( $M_* \sim 10^{9.5} M_\odot$  galaxies at  $z \approx 0.03$ ; Bordoloi

<sup>9</sup>The average  $W_r$  presented in table 3 of Prochaska et al. (2014) are calculated taking the non-detections at their measured values.

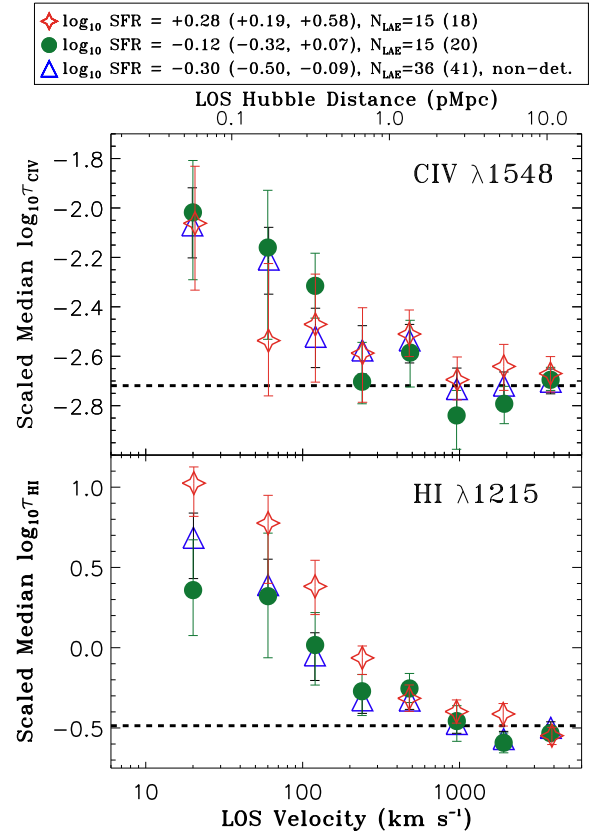


**Figure 16.** Similar to Fig. 9 but for three different SFR bins (all\_SFR\_non-det, blue; all\_SFR\_low, green; and all\_SFR\_high, red). The blue triangles represent the subsample of the UV-continuum-undetected objects. The median SFR values and 68 percentile ranges in the parentheses in the legends are for the LAEs contributing to the H I stack. The corresponding values for CIV stack can be found in Table 3. The H I profile is stronger and wider for the highest SFR bin, suggesting a strong SFR dependence. The noisier CIV profiles do not show any SFR dependence.

et al. 2014) with open triangles indicating upper limits. We divided the sample into two impact parameter bins. The bigger triangles mark the mean  $W_r(\text{CIV})$  at the median  $\rho$  of the two bins. As in Fig. 18, survival analysis is used to take into account the upper limits while calculating the means and the standard deviations (shown by the error bars). The small plus symbols denote the  $z \approx 0.15$  dwarf galaxy sample of Johnson et al. (2017, table 1). All except one are upper limits. The big plus symbol represents the mean  $W_r$  derived from survival analysis. The mean  $W_r(\text{CIV})$  values measured for the low- $z$  dwarf galaxy samples are broadly consistent with our measurements given the scatter in individual  $W_r$  values. The CIV  $W_r$ -profile for the LBGs shows a sharp decline at  $\approx 100$  pkpc which makes it consistent with our measurements. The  $W_r(\text{CIV})$  measurements of Turner et al. (2014) are somewhat higher compared to our measurements. Finally, at any given impact parameter probed by our sample, the  $W_r(\text{CIV})$  measured for the quasar hosts are at least an order of magnitude higher compared to our measurements. The quasar hosts also show significantly higher  $W_r(\text{CIV})$  compared to the COS-dwarf sample, as noted previously by Prochaska et al. (2014), and the LBG sample of Turner et al. (2014).

The five different samples plotted in Fig. 19 have halo masses ranging from  $\sim 10^{10.8}$  to  $10^{12.5} M_\odot$ . The galaxies in our sample have masses comparable to the dwarf galaxy sample of Johnson

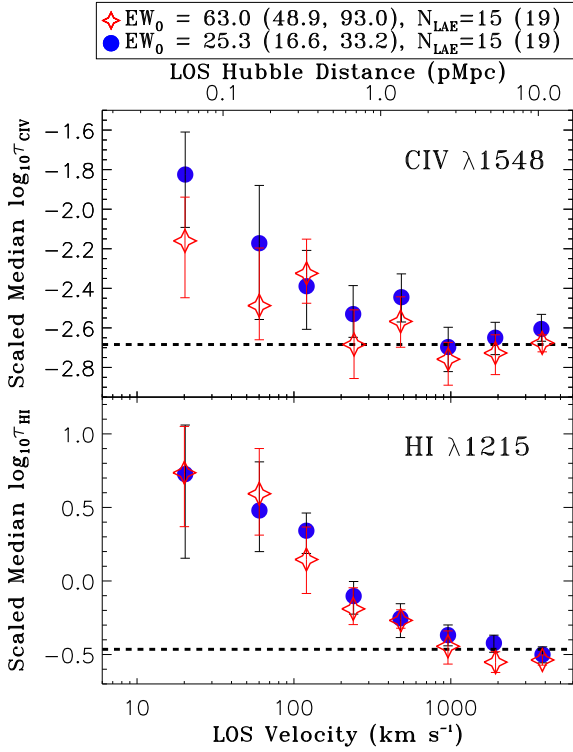


**Figure 17.** Similar to Fig. 9 but for two different  $EW_0$  bins (all  $EW_0$  low and all  $EW_0$  high). The median  $EW_0$  values and 68 percentile ranges in the parentheses in the legends are for the LAEs contributing to the H I stack. The corresponding values for C IV stack can be found in Table 3. No significant dependence on the  $EW_0$  of the Ly  $\alpha$  emission is seen in either H I or C IV absorption.

et al. (2017). The COS-Dwarf survey presents a sample of 43 dwarf galaxies at  $z \approx 0.03$  with a median  $M_* \approx 10^{9.5} M_\odot$  ( $M_h \sim 10^{11.5} M_\odot$ ) and a median  $R_{200} \approx 205$  pkpc. As mentioned earlier, the LBGs in the samples of Steidel et al. (2010) and Turner et al. (2014) have a median  $M_h \sim 10^{12.0} M_\odot$  (median  $R_{200} \approx 90$  pkpc). The quasar host galaxies studied by Prochaska et al. (2014) have the highest halo masses,  $M_h \sim 10^{12.5} M_\odot$ , corresponding to a median  $R_{200} \approx 145$  pkpc at  $z \approx 2$ . The right-hand panel of Fig. 19 shows the  $W_r(\text{C IV})$  as a function of normalized impact parameter, which minimizes the effects of different masses and redshifts for the different samples. Overall, the right-hand panel confirms the conclusions we derived from the left-hand panel. The  $W_r(\text{C IV})$  measured for the LAEs in our sample is now fully consistent with the LBG measurements of Turner et al. (2014).

## 5.2 Direct comparison with LBG optical depth profiles

In Section 5.1, we showed that at a given impact parameter, the mean  $W_r(\text{Ly } \alpha)$  for sightlines near LBGs are comparable to the sightlines near the LAEs in our sample, and marginally higher at  $\rho \lesssim 100$  pkpc (see the left-hand panel of Fig. 18). The LAEs, however, shows a significantly higher  $W_r(\text{Ly } \alpha)$  for  $\approx 3 - 8 \rho/R_{200}$  (see the right-hand panel of Fig. 18). The  $W_r(\text{C IV})$  measured for LBGs and LAEs are consistent with each other at a given  $\rho/R_{200}$  (see the right-hand panel of Fig. 19). Here, we directly compare the H I and C IV optical depth profiles for  $z \approx 2.3$  LBGs (Turner et al. 2014) and our LAEs.

As mentioned earlier, Turner et al. (2014) studied the CGM of 854 LBGs drawn from the KBSS survey using background quasars (see

Section 5.1). In Fig. 20, we reproduced the H I  $\lambda 1215$  and C IV  $\lambda 1548$  optical depth profiles for the LBG sample using table 5 of Turner et al. (2014). We also show the corresponding profiles obtained for our LAE sample, using the same logarithmic LOS velocity bins as used in their study. Moreover, for consistency, we used the same impact parameter range (i.e. 40–180 pkpc) as used by Turner et al. (2014, see their fig. 6). There are 43 (50) LAEs contributing to the H I (C IV) composites for our sample, which is  $\approx 2$  times larger than the number of LBGs (24) that contribute to the stacks.

It is evident from Fig. 20 that the H I absorption is significantly stronger and wider for the LBG sample compared to our LAE sample. C IV absorption, on the other hand, is only marginally stronger for LBGs. These findings are consistent with the conclusions we have drawn in Section 5.1 (see Fig. 18). The average  $W_r(\text{Ly } \alpha)$  for the first two impact parameter bins (40–180 pkpc) of Turner et al. (2014) is  $1000 \pm 220$  mÅ (see their table 8), which is larger than the corresponding average  $W_r(\text{Ly } \alpha)$  of  $810 \pm 138$  mÅ measured for the LAEs in our sample.

Three possible reasons that could cause such a difference in the CGM absorption are: (i) difference in mass, (ii) difference in SFR, and (iii) difference in redshift between the two samples. The galaxies from Turner et al. (2014) are UV-continuum selected ( $m_R \leq 25.5$ ), drawn from the KBSS survey (Steidel et al. 2010). As pointed out earlier, both the median mass and SFR of the LBG sample are at least an order of magnitude higher compared to our LAE sample. Moreover, the median redshift of our sample is 3.3, whereas the median redshift of the LBG sample is 2.3. Given the lack of evidence for redshift evolution in our sample (Section 4.5), the difference is unlikely due to the redshift difference. This conclusion, however, assumes that the lack of redshift evolution extends down to  $z \approx 2.3$ , which need not be true.

Owing to the lack of rest-frame optical data, we could not measure the stellar masses of the individual LAEs in our sample. We, however, have seen a strong SFR dependence for H I absorption in Section 4.8, which in turn can be driven by an underlying mass dependence if the LAEs in our sample follow a star-forming main-sequence relation as seen for low- $z$  galaxies. The higher halo mass (and the lower redshift) of the LBGs also imply that the fixed impact parameter range (40–180 pkpc) corresponds to smaller normalized impact parameters ( $\rho/R_{200}$ ) for the LBGs owing to larger virial radii. This can cause the observed differences as well.

## 5.3 Strong environment dependence

The strongest trend that we observed in this study is due to the environment (Section 4.3; Figs 8 and 9). The CGM absorption (both for H I and C IV) is significantly stronger for the ‘group’ galaxies compared to the isolated ones. The  $W_r$  measured for the stacked H I profile of the ‘group’ subsample is  $>2$  times stronger than the isolated subsample with a  $>4\sigma$  significance. The  $\sigma_v$  of the median stacked H I profile for the ‘group’ subsample is  $235 \pm 22$  km s $^{-1}$  ( $241 \pm 24$  km s $^{-1}$  for the mean stack), which is  $\approx 2.7$  times larger (with a  $>5\sigma$  significance) than that of the isolated subsample. Under pure Hubble flow, the  $\sigma_v$  of the ‘group’ subsample corresponds to a physical scale of  $\approx 700$  pkpc at  $z = 3.3$ , which is much larger than the typical group scale at these redshifts and exceeds the impact parameter range that we probe. On the other hand, the  $\sigma_v$  of  $\approx 240$  km s $^{-1}$  at  $z = 3.3$  would correspond to a halo mass of  $\sim 10^{12} M_\odot$ , provided it is dominated by dynamical motions.

Bordoloi et al. (2011) studied the effect of environment on Mg II absorbing gas at  $z \approx 0.7$  using stacking of background galaxy spectra. They found that the  $W_r$ -profile of group galaxies is considerably

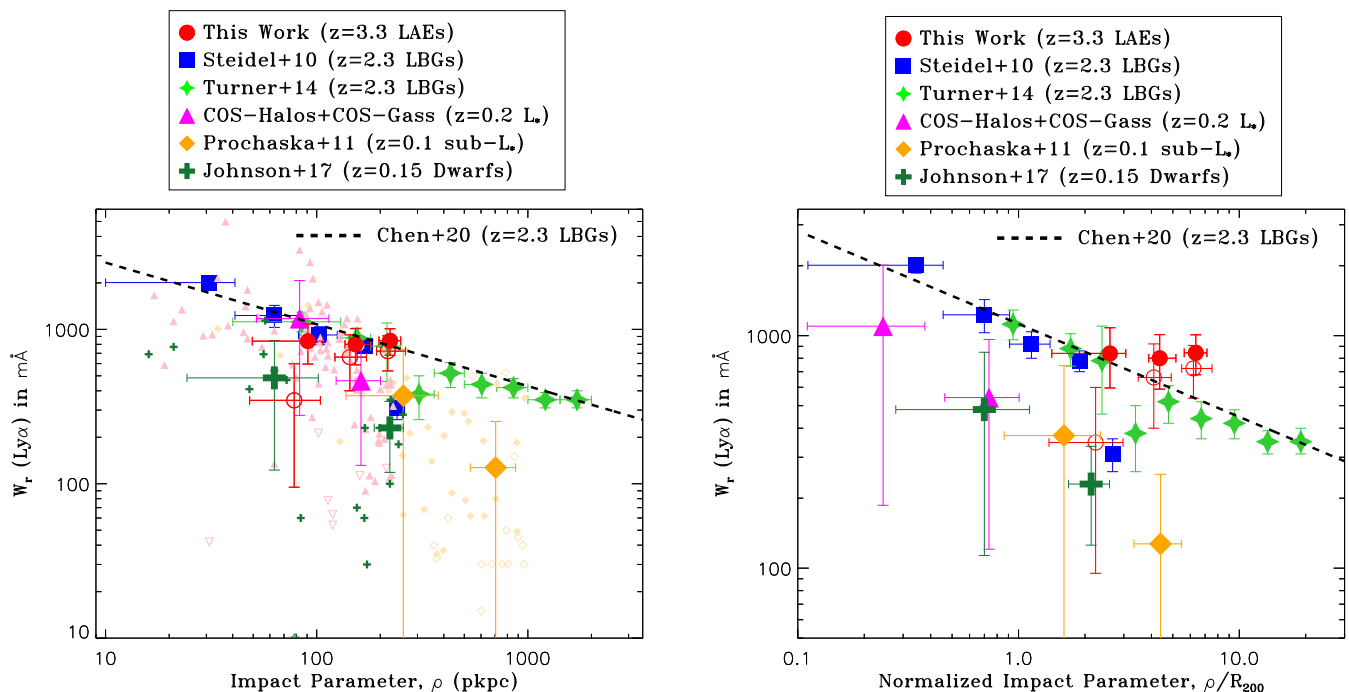


**Figure 18.** Left: Compilation of Ly  $\alpha$   $W_r$ -profiles. The red filled (open) circles mark the measurements of our full (‘isolated only’) sample. The equivalent widths are calculated from the *mean stacked* absorption profiles for our sample within a  $\pm 500$  km s $^{-1}$  velocity window (see Table A1). The small filled (open) triangles represent measurements (upper limits) for  $\sim L_*$  galaxies from the COS-Halos (Tumlinson et al. 2013) and COS-GASS (Borthakur et al. 2015) surveys at  $z \approx 0.2$ . The big magenta triangles provide the mean  $W_r$  of these data points split into two  $\rho$ -bins. The small filled (open) diamonds represent measurements (upper limits) for sub- $L_*$  galaxies from Prochaska et al. (2011) at  $z \approx 0.1$ . The big diamonds indicate the mean  $W_r$  of these data points for two  $\rho$ -bins. The small plus symbols represent the  $z \approx 0.15$  dwarf galaxy sample of Johnson et al. (2017). The mean  $W_r$  values of the two  $\rho$ -bins are shown by the big plus symbols. The error bars on the triangles, diamonds, and plus symbols indicate the standard deviations. Survival statistics is used to take into account the censored data points (upper limits) while calculating the mean and standard deviations. The blue squares represent measurements for  $z \approx 2.3$  LBGs (Steidel et al. 2010). The green star symbols are from Turner et al. (2014), and the dashed straight line represents the best-fitting power-law relation from Chen et al. (2020) obtained from a significantly larger sample size from the same survey. The Ly  $\alpha$  equivalent widths measured for the LAEs in our sample are comparable to those measured for  $z \approx 2.3$  LBGs and  $z \approx 0.2 L_*$  galaxies, but considerably higher than the measurements for sub- $L_*$  and dwarf galaxies at low- $z$ . Right: The same as the left but the  $W_r$  values are plotted against the impact parameters normalized by the corresponding median  $R_{200}$  values (see text). The environments of LAEs are significantly more rich in H I gas compared to LBGs at  $z \approx 2.3$  and sub- $L_*$  and dwarf galaxies at low- $z$  at a given normalized impact parameter.

flatter compared to that of the isolated galaxies, so that at any given impact parameter at  $\rho > 50$  pkpc, the  $W_r(\text{Mg II})$  is significantly higher for the group galaxies (see also Nielsen et al. 2018). More recently, using a sample of 228 MUSE-detected galaxies at  $z \approx 0.8 - 1.5$ , Dutta et al. (2020) reported five times stronger absorption and three times higher covering fraction of Mg II for group galaxies (two or more galaxies within 500 kpc and 500 km s $^{-1}$ ). A simple model that assumes that the Mg II absorption of a group can be represented by the superposition of the absorption of individual member galaxies successfully reproduces the  $W_r$ -profile for the group galaxies. Nielsen et al. (2018) showed that while such a simple model predicts the right  $W_r$  for groups, it overpredicts the absorption kinematics.

Recently, using a handful of galaxy groups (more than two galaxies within 400 kpc and 400 km s $^{-1}$ ), Fossati et al. (2019) showed that the Mg II absorption in groups is stronger than what is typically seen for more isolated galaxies at comparable impact parameters leading to a rather flat  $W_r$ -profile (see also Chen et al. 2010; Dutta et al. 2020). They argued that stripping of metal-rich gas from the individual haloes due to gravitational interactions between the member galaxies in a group gives rise to the large cross-section for Mg II. Here, we emphasize that in most of these Mg II absorber studies discussed above, ‘group’ does not necessarily mean a virialized structure. It is rather a measure of overdensity.

The strong environmental dependence we observe for H I and C IV is consistent with what various authors have seen for Mg II. However, we point out that for the majority of our LAEs, the impact parameters (median  $\rho \approx 165$  pkpc) are larger than the virial radii, which are only a few tens of kpc. It is likely that the LAEs in ‘group’ subsample reside in relatively more massive haloes. The hierarchical nature of cosmic structures naturally facilitates more gas in such environments. The metallicity of the absorbing gas, which will be presented in future work, will provide crucial insights into the nature of the absorbers.

Using a C IV-absorption-selected sample, Burchett et al. (2016) found that the detection rate of C IV is lower for group ( $M_h > 10^{12.5} M_\odot$ ) galaxies at  $z < 0.015$ . H I, on the other hand, did not show any dependence on mass or environment. Indeed, at such high halo masses, a decline in Mg II equivalent width has been reported by Bouché et al. (2006) from the cross-correlation of Mg II absorbers with luminous red galaxies (see also Lundgren et al. 2009). However, we point out that  $10^{12.5} M_\odot$  is considerably larger than the halo masses of the LAEs in our sample ( $\sim 10^{11} M_\odot$ ).

Johnson, Chen & Mulchaey (2015) studied environmental effects for O VI somewhat beyond the virial radii of individual galaxies at low redshift ( $z \approx 0.2$ ). They found a relatively enhanced detection rate for O VI absorption around galaxies with nearby neighbours, and suggested that galaxy interactions in the form of ram-pressure and tidal stripping can distribute metal enriched gas out to distances well

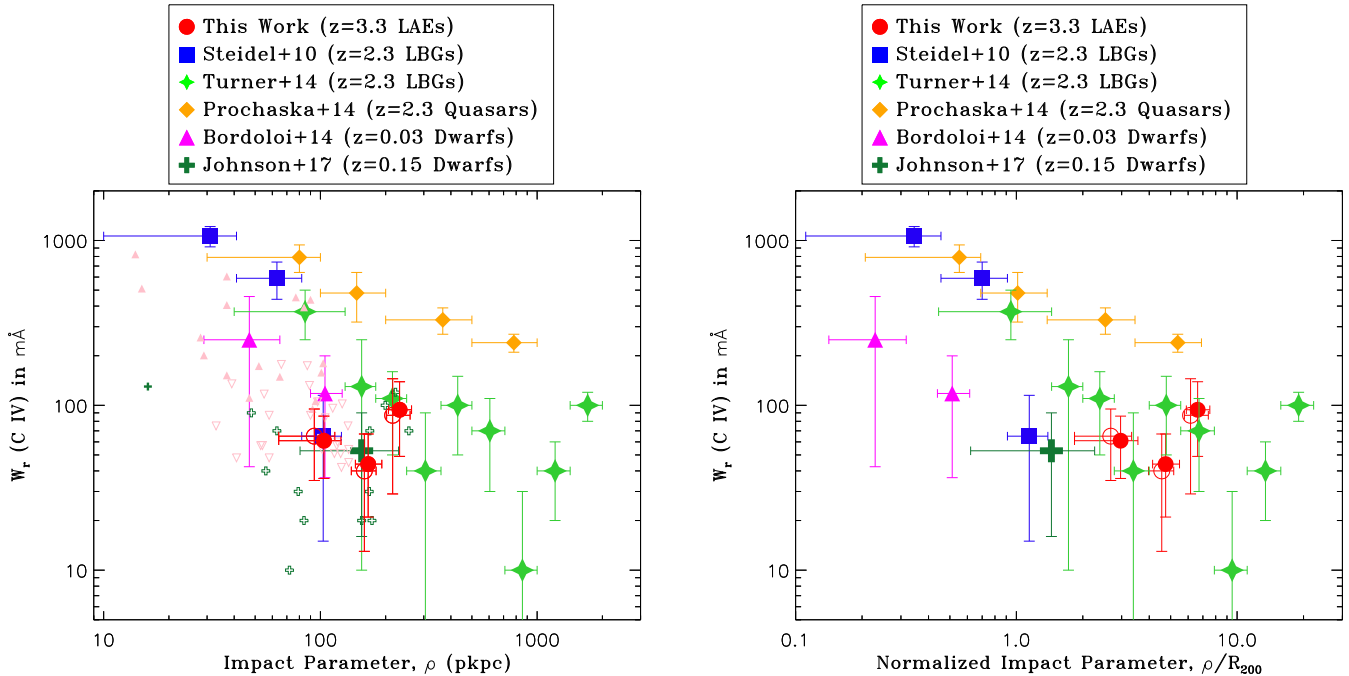


**Figure 19.** Left: Compilation of C IV  $W_r$ -profiles. The equivalent widths for our sample are calculated from the *mean stacked* absorption profiles within a  $\pm 500 \text{ km s}^{-1}$  velocity window (see Table A2). The filled and open red circles are for the full and ‘isolated only’ samples, respectively. The big magenta triangles indicate the mean  $W_r$  of the COS-Dwarf sample (Bordoloi et al. 2014) divided into two impact parameter bins. The individual detections (upper limits) are shown by the small solid (open) triangles. The small plus symbols represent the  $z \approx 0.15$  dwarf galaxy sample of Johnson et al. (2017), with open symbols indicating upper limits. The big plus symbol indicates the mean  $W_r$ . Survival analysis is used to take into account the censored data points (upper limits) while calculating the mean and standard deviations (error bar along y-axis) for both the dwarf galaxy samples. The blue squares and green star symbols represent measurements of  $z \approx 2.3$  LBGs from Steidel et al. (2010) and Turner et al. (2014), respectively. The orange diamonds indicate observations of  $z \approx 2$  quasar host galaxies from Prochaska, Lau & Hennawi (2014). The error bars along x-axis for the blue squares, green stars, and orange diamonds represent the full range, and 68 percentiles for the red circles, magenta triangles, and the plus symbol. Right: The same as the left but the  $W_r$  values are plotted against the impact parameters normalized by the corresponding median  $R_{200}$  values (see text). For a fixed normalized impact parameter, our  $W_r(\text{C IV})$  measurements are comparable to those of the  $z \approx 2.3$  LBGs and low- $z$  dwarf galaxies, but considerably lower compared to the  $z \approx 2.3$  quasar host galaxies.

beyond individual haloes. Finally, Pointon et al. (2017) studied the effect of group environment on circumgalactic O VI absorption at  $z \approx 0.2$ , using a sample of 18 galaxy groups (two or more galaxies with an LOS velocity difference smaller than  $1000 \text{ km s}^{-1}$  and located within 350 pkpc of the background quasars). They found a  $3\sigma$  result that the average  $W_r(\text{O VI})$  for the group galaxies are smaller than for the isolated ones. But, they find that the covering fractions of O VI are comparable between the two samples. They suggested that O VI traces warm/hot gas in the halo, which is too highly ionized owing to the higher virial temperature for the groups. The H I and C IV as studied here are tracers of cool, photoionized gas (see e.g. Muzahid et al. 2012) which are not particularly sensitive to the virial temperature.

#### 5.4 Strong SFR dependence

SF-driven outflows are thought to play an important role in determining the chemical, kinematical, and physical structure of the CGM. We noticed a strong SFR dependence for the H I absorption in Section 4.8 (see Figs 15 and 16), with the highest SFR bin showing significantly stronger and wider absorption compared to the lower SFR bins. No significant SFR dependence is seen when we limited our sample to ‘isolated only’ LAEs. However, in that case we do lose a significant number (about half) of the high SFR LAEs with  $\log \text{SFR}/M_{\odot} \text{ yr}^{-1} > 0.1$ , which reduces the dynamic range and the median SFR of the high-SFR bin. We thus believe that the strong

SFR dependence seen for the full sample cannot be entirely due to the underlying environmental dependence.

The SFRs calculated from UV continua has a characteristic time-scale of  $\approx 100 \text{ Myr}$  (Kennicutt 1998). If the observed trend of enhanced H I in the CGM of high SFR galaxies is owing to the wind materials entrained by SFR-driven outflows, then the wind velocity required to travel a distance of 165 pkpc (median  $\rho$ ) is  $\approx 165 \text{ pkpc}/100 \text{ Myr} \approx 1600 \text{ km s}^{-1}$ . In models of momentum-driven outflows, the wind speed scales as the halo circular velocity (Murray, Quataert & Thompson 2005; Heckman et al. 2015). The expected circular velocity for the low-mass galaxies in our sample is only  $\approx 120 \text{ km s}^{-1}$ , which is an order of magnitude lower than the velocity required for a causal connection between wind driven by the observed star formation and CGM absorption. While wind velocities much greater than the circular velocity have been observed on interstellar medium (ISM) scales (e.g. Steidel et al. 2010), it is unclear that such high velocities are maintained out to distances comparable to or larger than the halo virial radius, particularly since the mass in the CGM is expected to exceed that in the ISM by a large factor.

In other words, the distance travelled by an outflow in 100 Myr with a speed of  $\approx 120 \text{ km s}^{-1}$  is only  $\approx 12 \text{ pkpc}$ , which is an order of magnitude lower than the median impact parameter of our sample. Unless the SFR has been high for time-scales  $\gg 100 \text{ Myr}$ , the observed trend cannot be explained by outflows associated with the star formation episode that we observe. This is also consistent with the lack of a trend seen for C IV.

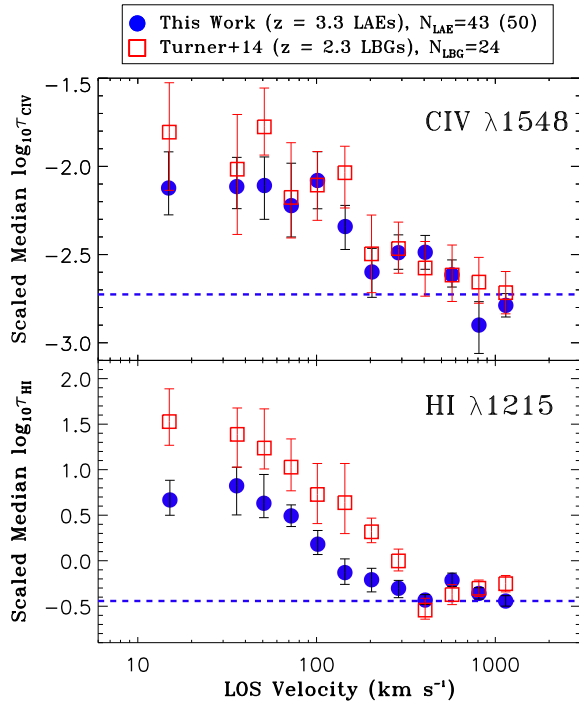


**Figure 20.** Comparison of the median stacked optical depth profiles of our LAEs and  $z \approx 2.3$  LBGs for impact parameters of 40–180 pkpc. Bottom: The median H I  $\lambda 1215$  optical depth profile for our LAE sample is shown by the blue circles. The corresponding median optical depth in random regions is shown by the blue dashed line. The median Ly  $\alpha$  optical depth profile for LBGs (Turner et al. 2014) is shown by the red squares, after linearly scaling to the same background level as indicated by the dashed line. In both cases, the  $1\sigma$  confidence intervals are calculated from 1000 bootstrap realizations of the corresponding galaxy samples. The number of galaxies contributing to the plots are indicated in the legends. Top: Same as the bottom but for the C IV  $\lambda 1548$  line. The number in parentheses in the legend is the number of LAEs contributing to the C IV stack. For a fixed impact parameter range (i.e. 40–180 pkpc), the CGM of LBGs appears to be more H I-rich. C IV, on the other hand, shows only a marginal difference.

We instead speculate that the higher SFR is the consequence of the availability of more cool, neutral gas in the CGM. In particular, the observed SFR dependence can be explained by an underlying mass dependence provided LAEs at these redshifts follow a star-forming main-sequence relation like the normal low- $z$  galaxy population. Alternatively, galaxies of a fixed mass whose environment is more H I-rich, may also tend to be more gas rich themselves and hence have higher SFRs.

## 6 SUMMARY

We presented the first results of the MUSEQuBES survey on the CGM of 96 LAEs with redshifts in the range  $z = 2.9 - 3.8$  (median  $z = 3.3$ ). This is the first study characterizing the gaseous environment of LAEs using background quasars on relatively small scales (impact parameters  $\rho = 16 - 315$  pkpc; median  $\rho = 165$  pkpc) with a statistically significant sample. The LAEs are detected within  $1 \text{ arcsec} \times 1 \text{ arcsec}$  fields centred on bright  $z = 3.6 - 3.9$  quasars with the MUSE integral field spectrograph on the VLT. Our MUSE exposures are deep, on average 6 h per field, yielding a relatively faint sample of LAEs with Ly  $\alpha$  luminosities  $\sim 10^{42} \text{ erg s}^{-1}$ . The SFRs are estimated from the rest-frame UV continua, which we detect with  $>5\sigma$  confidence for about half the

sample. Neglecting dust corrections, we obtain  $\text{SFR} \sim 1 M_{\odot} \text{ yr}^{-1}$ , which for main-sequence galaxies corresponds to stellar masses of  $\sim 10^{8.6} M_{\odot}$ . Subhalo abundance matching results suggest that this stellar mass corresponds to a halo mass of only  $\sim 10^{11} M_{\odot}$ . High-quality quasar spectra were obtained using over 250 h of (mostly archival) observations with the UVES Echelle spectrograph on the VLT, as well as some Keck/HIRES observations to fill in gaps in the UVES coverage.

We used mean and median spectral stacking to investigate possible trends between LAE properties and the CGM absorption. We focused on the H I and C IV absorption lines, since these are the only two lines detected at  $>3\sigma$  significance in the composite spectrum. In order to minimize contamination from unrelated absorption and to correct for possible line saturation, we used pixel optical depths recovered using the PYTHON module PODPY (Turner et al. 2014), though this only affects our quantitative conclusions. Since the Ly  $\alpha$  emission peaks do not provide the systemic redshifts owing to the resonant nature of the Ly  $\alpha$  line, we used the empirical relation between velocity offset (with respect to the systemic redshift) and FWHM as obtained in Muzahid et al. (2020) to correct the Ly  $\alpha$  redshifts.

Our main findings are:

(i) There is significant excess H I and C IV absorption near the LAEs out to  $500 \text{ km s}^{-1}$  (Fig. 6) and at least  $\approx 250$  pkpc (corresponding to  $\approx 7$  virial radii) (Figs 10 and 11). At  $\lesssim 30 \text{ km s}^{-1}$  from the galaxies the median H I and C IV optical depths are enhanced by an order of magnitude (Fig. 6).

(ii) A strong environmental dependence is seen for both H I and C IV (Figs 8 and 9). The absorption is significantly stronger near the  $\approx 1/3$  of our LAEs that are part of a ‘group’ (multiple LAEs in the MUSE FoV within  $\pm 500 \text{ km s}^{-1}$ ) than near isolated LAEs. We suggest that the large-scale structure around more massive haloes, hosting multiple LAEs, is the cause of the enhanced CGM absorption for ‘group’ galaxies.

(iii) We searched for a dependence on impact parameter of the optical depth profile as a function of velocity (Fig. 10) and of the equivalent widths in fixed velocity windows (Fig. 11). We do not detect any significant, systematic dependence of either the H I or C IV absorption on transverse distance (over the range  $\approx 50 - 250$  pkpc). This is true for both the full sample and the isolated LAEs. We argued that the lack of a trend with impact parameter for the isolated LAEs could in part be due to the fact that galaxies near the edge of the FoV may belong to groups whose members reside outside it.

(iv) Comparing subsamples of isolated LAEs with median redshifts differing by  $\Delta z \approx 0.4$ , we do not find any evidence for redshift evolution (Fig. 12).

(v) Focusing on the isolated LAEs, we do not detect any significant dependence of the absorption on the luminosity (Fig. 13), FWHM (Fig. 14), or equivalent width (Fig. 17) of the Ly  $\alpha$  emission line when we compare subsamples that differ by factors of  $\approx 3$ , 1.5, and 2 in  $L(\text{Ly } \alpha)$ , FWHM, and  $EW_0$ , respectively.

(vi) The H I absorption at  $\lesssim 100 \text{ km s}^{-1}$  from the LAE increases with the SFR, but the C IV absorption does not show any trend with SFR (Figs 15 and 16). Using simple velocity/time-scale arguments, we conclude that the enhanced H I absorption seen for the high-SFR subsample cannot be due to the material entrained by SFR-driven winds. Instead, we favour a scenario in which galaxies surrounded by more cool neutral gas, either because the galaxies are more massive or because the H I fraction is relatively high in their environments, tend to have higher SFRs owing to the readily available fuel for star formation. We do not see any significant trend with SFR for the isolated LAEs, but this may owe to the smaller number of isolated

high-SFR LAEs reducing the dynamic range in SFR. Nevertheless, this does suggest the possibility that the trend seen in the full sample may be partly driven by the underlying environmental dependence.

(vii) Direct comparison of the excess optical depth profiles as a function of velocity for impact parameters of 40–180 pkpc with those of  $z \approx 2.3$  LBGs shows that the environments of LBGs are more enhanced in H I than is the case for our LAEs (Fig. 20). We argue that the order of magnitude higher SFRs and halo masses of the LBGs are the most likely cause for the enhanced H I absorption. However, no significant differences are found for C IV.

(viii) At a fixed impact parameter, the equivalent widths of the H I absorption for our sample are larger than observed for low- $z$  dwarf/sub- $L_*$  galaxies, but comparable to those of  $\approx L_*$  galaxies at low  $z$  and  $z \approx 2.3$  LBGs. However, we find that at a given normalized impact parameter ( $\rho/R_{200}$ ) the LAEs show stronger Ly  $\alpha$  absorption compared to LBGs (Fig. 18).

(ix) A comparison with C IV equivalent width profiles from the literature indicates that quasar-host haloes are significantly richer in C IV compared to LAEs (and LBGs). The C IV equivalent widths measured near the LAEs are, however, comparable to those for low- $z$  dwarf galaxies and  $z \approx 2.3$  LBGs (Fig. 19).

This is the second paper reporting results from the high- $z$  MUSEQuBES survey and the first focusing on the properties of the CGM of LAEs. Our results extend studies of the gas around high- $z$  galaxies to much lower galaxy masses than were probed by previous surveys, thus extending observational constraints from rare objects such as quasars and the progenitors of massive galaxies to the ubiquitous but faint progenitors of the galaxies that dominate the cosmic stellar mass density. In future work, we plan to extend our analysis from flux statistics to measurements of column densities and line widths. We also intend to study some individual systems in more detail.

## ACKNOWLEDGEMENTS

We would like to thank the anonymous referee for the useful comments which improved the clarity of the paper. This work is partly funded by Vici grant 639.043.409 from the Dutch Research Council (NWO). SM thanks the Alexander von Humboldt-Stiftung (Germany). SM also thanks Monica Turner, Lorrie Straka, Marijke Segers, and Peter Mitchell for useful discussion. SC gratefully acknowledges support from Swiss National Science Foundation grant PP00P2\_190092 and from the European Research Council (ERC) under the European Union's Horizon 2020 research and innovation programme grant agreement No 864361. NB acknowledges support from the ANR 3DGasFlows (ANR-17-CE31-0017).

## DATA AVAILABILITY

The data underlying this article are available in ESO (<http://archive.eso.org/cms.html>) and Keck (<https://www2.keck.hawaii.edu/koa/public/koa.php>) public archives.

## REFERENCES

Adelberger K. L., Shapley A. E., Steidel C. C., Pettini M., Erb D. K., Reddy N. A., 2005, *ApJ*, 629, 636  
 Aguirre A., Dow-Hygelund C., Schaye J., Theuns T., 2008, *ApJ*, 689, 851  
 Bacon R. et al., 2010, in McLean I. S., Ramsay S. K., Takami H., eds, Proc. SPIE Conf. Ser. Vol. 7735, Ground-Based and Airborne Instrumentation for Astronomy III. SPIE, Bellingham, p. 773508

Bacon R. et al., 2015, *A&A*, 575, A75  
 Bacon R. et al., 2021, *A&A*, 647, A107  
 Behroozi P., Wechsler R. H., Hearin A. P., Conroy C., 2019, *MNRAS*, 488, 3143  
 Bielby R. M. et al., 2017, *MNRAS*, 471, 2174  
 Bielby R. M. et al., 2020, *MNRAS*, 493, 5336  
 Bordoloi R. et al., 2011, *ApJ*, 743, 10  
 Bordoloi R. et al., 2014, *ApJ*, 796, 136  
 Borisova E. et al., 2016, *ApJ*, 831, 39  
 Borthakur S. et al., 2015, *ApJ*, 813, 46  
 Bouché N., Murphy M. T., Péroux C., Csabai I., Wild V., 2006, *MNRAS*, 371, 495  
 Burchett J. N. et al., 2016, *ApJ*, 832, 124  
 Cai Z. et al., 2019, *ApJS*, 245, 23  
 Cantalupo S., Arrigoni-Battaia F., Prochaska J. X., Hennawi J. F., Madau P., 2014, *Nature*, 506, 63  
 Cantalupo S. et al., 2019, *MNRAS*, 483, 5188  
 Chabrier G., 2003, *PASP*, 115, 763  
 Chen H.-W., Helsby J. E., Gauthier J.-R., Shtetman S. A., Thompson I. B., Tinker J. L., 2010, *ApJ*, 714, 1521  
 Chen Y. et al., 2020, *MNRAS*, 499, 1721  
 Cowie L. L., Songaila A., 1998, *Nature*, 394, 44  
 Crighton N. H. M. et al., 2011, *MNRAS*, 414, 28  
 Díaz C. G., Ryan-Weber E. V., Cooke J., Koyama Y., Ouchi M., 2015, *MNRAS*, 448, 1240  
 Díaz C. G., Ryan-Weber E. V., Karman W., Caputi K. I., Salvadori S., Crighton N. H., Ouchi M., Vanzella E., 2021, *MNRAS*, 502, 2645  
 Dutta R. et al., 2020, *MNRAS*, 499, 5022  
 Fossati M. et al., 2019, *MNRAS*, 490, 1451  
 Fumagalli M., Cantalupo S., Dekel A., Morris S. L., O'Meara J. M., Prochaska J. X., Theuns T., 2016, *MNRAS*, 462, 1978  
 Heckman T. M., Alexandroff R. M., Borthakur S., Overzier R., Leitherer C., 2015, *ApJ*, 809, 147  
 Inami H. et al., 2017, *A&A*, 608, A2  
 Johnson S. D., Chen H.-W., Mulchaey J. S., 2015, *MNRAS*, 449, 3263  
 Johnson S. D., Chen H.-W., Mulchaey J. S., Schaye J., Straka L. A., 2017, *ApJ*, 850, L10  
 Keeney B. A. et al., 2017, *ApJS*, 230, 6  
 Kennicutt R. C. Jr, 1998, *ARA&A*, 36, 189  
 Leclercq F. et al., 2017, *A&A*, 608, A8  
 Lofthouse E. K. et al., 2020, *MNRAS*, 491, 2057  
 Lundgren B. F. et al., 2009, *ApJ*, 698, 819  
 Mackenzie R. et al., 2019, *MNRAS*, 487, 5070  
 Marino R. A. et al., 2018, *ApJ*, 859, 53  
 Momose R. et al., 2021, *ApJ*, 909, 117  
 Moster B. P., Naab T., White S. D. M., 2013, *MNRAS*, 428, 3121  
 Mukae S. et al., 2017, *ApJ*, 835, 281  
 Murphy M. T., Kacprzak G. G., Savorgnan G. A. D., Carswell R. F., 2019, *MNRAS*, 482, 3458  
 Murray N., Quataert E., Thompson T. A., 2005, *ApJ*, 618, 569  
 Muzahid S., Srianand R., Bergeron J., Petitjean P., 2012, *MNRAS*, 421, 446  
 Muzahid S. et al., 2020, *MNRAS*, 496, 1013  
 Nielsen N. M., Kacprzak G. G., Pointon S. K., Churchill C. W., Murphy M. T., 2018, *ApJ*, 869, 153  
 Nielsen N. M., Kacprzak G. G., Pointon S. K., Murphy M. T., Churchill C. W., Davé R., 2020, *ApJ*, 904, 164  
 O'Meara J. M. et al., 2015, *AJ*, 150, 111  
 Peeples M. S., Werk J. K., Tumlinson J., Oppenheimer B. D., Prochaska J. X., Katz N., Weinberg D. H., 2014, *ApJ*, 786, 54  
 Pointon S. K., Nielsen N. M., Kacprzak G. G., Muzahid S., Churchill C. W., Charlton J. C., 2017, *ApJ*, 844, 23  
 Prochaska J. X., Weiner B., Chen H.-W., Mulchaey J., Cooksey K., 2011, *ApJ*, 740, 91  
 Prochaska J. X., Lau M. W., Hennawi J. F., 2014, *ApJ*, 796, 140  
 Rakic O., Schaye J., Steidel C. C., Rudie G. C., 2011, *MNRAS*, 414, 3265  
 Rakic O., Schaye J., Steidel C. C., Rudie G. C., 2012, *ApJ*, 751, 94

Rakic O., Schaye J., Steidel C. C., Booth C. M., Dalla Vecchia C., Rudie G. C., 2013, *MNRAS*, 433, 3103

Rudie G. C. et al., 2012, *ApJ*, 750, 67

Rudie G. C., Steidel C. C., Pettini M., Trainor R. F., Strom A. L., Hummels C. B., Reddy N. A., Shapley A. E., 2019, *ApJ*, 885, 61

Schaye J., Aguirre A., Kim T.-S., Theuns T., Rauch M., Sargent W. L. W., 2003, *ApJ*, 596, 768

Schaye J. et al., 2015, *MNRAS*, 446, 521

Steidel C. C., Erb D. K., Shapley A. E., Pettini M., Reddy N., Bogosavljević M., Rudie G. C., Rakic O., 2010, *ApJ*, 717, 289

Steidel C. C. et al., 2014, *ApJ*, 795, 165

Trainor R. F., Steidel C. C., 2012, *ApJ*, 752, 39

Trainor R. F., Steidel C. C., Strom A. L., Rudie G. C., 2015, *ApJ*, 809, 89

Tumlinson J. et al., 2011, *ApJ*, 733, 111

Tumlinson J. et al., 2013, *ApJ*, 777, 59

Tumlinson J., Peeples M. S., Werk J. K., 2017, *ARA&A*, 55, 389

Turner M. L., Schaye J., Steidel C. C., Rudie G. C., Strom A. L., 2014, *MNRAS*, 445, 794

Turner M. L., Schaye J., Steidel C. C., Rudie G. C., Strom A. L., 2015, *MNRAS*, 450, 2067

Turner M. L., Schaye J., Crain R. A., Rudie G., Steidel C. C., Strom A., Theuns T., 2017, *MNRAS*, 471, 690

Umehata H. et al., 2019, *Science*, 366, 97

Verhamme A., Orlitová I., Schaerer D., Hayes M., 2015, *A&A*, 578, A7

Weilbacher P. M. et al., 2020, *A&A*, 641, A28

Werk J. K., Prochaska J. X., Thom C., Tumlinson J., Tripp T. M., O'Meara J. M., Peeples M. S., 2013, *ApJS*, 204, 17

Werk J. K. et al., 2014, *ApJ*, 792, 8

Wisotzki L. et al., 2016, *A&A*, 587, A98

Zahedy F. S., Rauch M., Chen H.-W., Carswell R. F., Stalder B., Stark A. A., 2019, *MNRAS*, 486, 1392

## SUPPORTING INFORMATION

Supplementary data are available at *MNRAS* online.

**Figure S1.** Shows impact parameter dependence for the full sample.

**Figure S2.** Shows impact parameter dependence for the 'isolated only' sample.

**Figure S3.** Shows redshift-dependence for the 'isolated only' sample.

**Figure S4.** Shows ( $L_y$ )-dependence for the 'isolated only' sample

**Figure S5.** Shows FWHM-dependence for the 'isolated only' sample

**Figure S6.** Shows  $EW_0$ -dependence for the full sample

Please note: Oxford University Press is not responsible for the content or functionality of any supporting materials supplied by the authors. Any queries (other than missing material) should be directed to the corresponding author for the article.

## APPENDIX A: MEASUREMENTS PERFORMED ON THE STACKED PROFILES

Table A1 presents the summary of measurements performed on the HI stacks.

Table A2 presents the summary of measurements performed on the CIV stacks.

**Table A1.** Measurements performed on the H I stacks.

Sample	$V_{\text{offset}}$ (km s <sup>-1</sup> )		$\sigma_v$ (km s <sup>-1</sup> )		$W_r$ (Å)		$W_r$ (Å)		$\log_{10} N(\text{H I})/\text{cm}^{-2}$	
	Mean	Median	Mean	Median	Mean	Median	Mean	Median	Mean	Median
(1)	(2)	(3)	(4)	(5)	(6)	(7)	(8)	(9)	(10)	(11)
all	-8 ± 11	-2 ± 10	141 ± 11	128 ± 10	0.709 ± 0.085	1.186 ± 0.147	0.823 ± 0.120	1.323 ± 0.182	14.12 ± 0.05	14.39 ± 0.06
all_environment_iso	-5 ± 11	-2 ± 11	99 ± 11	85 ± 10	0.550 ± 0.107	0.877 ± 0.189	0.573 ± 0.140	0.927 ± 0.218	14.00 ± 0.08	14.23 ± 0.10
all_environment_group	2 ± 22	9 ± 21	241 ± 24	235 ± 22	1.119 ± 0.122	1.773 ± 0.150	1.467 ± 0.210	2.279 ± 0.305	14.31 ± 0.05	14.62 ± 0.06
all_ρ_low <sup>d</sup>	11 ± 18	11 ± 17	117 ± 20	127 ± 18	0.732 ± 0.169	1.339 ± 0.267	0.839 ± 0.243	1.478 ± 0.353	14.13 ± 0.10	14.43 ± 0.10
all_ρ_mid	-33 ± 13	-40 ± 12	105 ± 13	95 ± 12	0.705 ± 0.131	1.115 ± 0.195	0.800 ± 0.211	1.283 ± 0.267	14.11 ± 0.08	14.37 ± 0.09
all_ρ_high	18 ± 18	20 ± 17	145 ± 18	123 ± 14	0.725 ± 0.137	1.196 ± 0.232	0.844 ± 0.165	1.311 ± 0.259	14.12 ± 0.08	14.38 ± 0.09
iso_ρ_low	-4 ± 25	6 ± 18	94 ± 26	77 ± 20	0.469 ± 0.220	0.877 ± 0.404	0.347 ± 0.252	0.869 ± 0.442	13.94 ± 0.20	14.20 ± 0.22
iso_ρ_mid	-28 ± 12	-28 ± 11	93 ± 12	95 ± 13	0.721 ± 0.164	1.120 ± 0.226	0.661 ± 0.261	1.140 ± 0.327	14.12 ± 0.10	14.32 ± 0.12
iso_ρ_high	49 ± 24	43 ± 21	131 ± 24	96 ± 17	0.537 ± 0.155	0.792 ± 0.256	0.723 ± 0.185	0.977 ± 0.272	13.99 ± 0.13	14.25 ± 0.12
iso_z_peak_low <sup>b</sup>	-10 ± 16	-17 ± 16	108 ± 16	82 ± 14	0.544 ± 0.127	0.815 ± 0.225	0.672 ± 0.175	0.970 ± 0.271	14.00 ± 0.10	14.25 ± 0.12
iso_z_peak_high	5 ± 13	3 ± 12	84 ± 14	82 ± 13	0.546 ± 0.163	0.995 ± 0.283	0.446 ± 0.202	0.923 ± 0.325	14.00 ± 0.13	14.23 ± 0.15
iso_L(Ly α)_low	-24 ± 19	-29 ± 18	100 ± 18	85 ± 15	0.448 ± 0.156	0.811 ± 0.273	0.440 ± 0.216	0.845 ± 0.330	13.92 ± 0.15	14.19 ± 0.17
iso_L(Ly α)_high	9 ± 12	6 ± 11	90 ± 12	86 ± 12	0.645 ± 0.129	0.955 ± 0.226	0.697 ± 0.153	1.047 ± 0.244	14.07 ± 0.09	14.28 ± 0.10
iso_FWHM_low	-49 ± 21	-47 ± 22	113 ± 20	102 ± 18	0.518 ± 0.156	0.910 ± 0.293	0.518 ± 0.223	0.927 ± 0.354	13.98 ± 0.13	14.23 ± 0.17
iso_FWHM_high	19 ± 11	11 ± 12	83 ± 11	83 ± 11	0.574 ± 0.137	0.900 ± 0.200	0.632 ± 0.157	1.024 ± 0.219	14.02 ± 0.10	14.27 ± 0.09
all_SFR_non-det <sup>c</sup>	2 ± 12	11 ± 11	105 ± 12	94 ± 10	0.660 ± 0.114	0.983 ± 0.182	0.788 ± 0.176	1.121 ± 0.255	14.08 ± 0.08	14.31 ± 0.10
all_SFR_low <sup>d</sup>	-47 ± 18	-50 ± 17	87 ± 18	85 ± 15	0.592 ± 0.155	1.003 ± 0.222	0.754 ± 0.248	1.268 ± 0.322	14.04 ± 0.11	14.37 ± 0.11
all_SFR_high	17 ± 19	30 ± 15	154 ± 19	161 ± 16	1.042 ± 0.185	1.638 ± 0.219	1.080 ± 0.274	1.822 ± 0.301	14.28 ± 0.08	14.52 ± 0.07
all_EW <sub>0</sub> _low	-48 ± 19	-26 ± 20	126 ± 18	154 ± 18	0.801 ± 0.173	1.372 ± 0.249	0.912 ± 0.292	1.660 ± 0.356	14.17 ± 0.09	14.48 ± 0.09
all_EW <sub>0</sub> _high	43 ± 22	44 ± 14	149 ± 22	132 ± 14	0.791 ± 0.188	1.314 ± 0.259	0.909 ± 0.244	1.566 ± 0.298	14.16 ± 0.10	14.46 ± 0.08

*Notes.* (1) The sample, as defined in Table 3, used for stacking. (2) and (3) The  $V_{\text{offset}}$  (line centroids) measured for the mean and median stack profiles, respectively. (4) and (5) The line widths obtained from single-component Gaussian fits to the mean and median stacked profiles, respectively. A spectral range of  $[-500, +500]$  km s<sup>-1</sup> is used for Gaussian fitting, unless specified otherwise. The uncertainties in columns 2–5 are the fitting errors determined from the error spectra. The error spectra are obtained from the standard deviations of the mean/median flux distributions of 1000 bootstrap samples. (6) and (7) Rest-frame equivalent widths of the line measured within  $\pm 300$  km s<sup>-1</sup> of the line centroid of the mean and median stacked profiles, respectively. (8) and (9) Rest-frame equivalent width of the line measured within  $\pm 500$  km s<sup>-1</sup> of the line centroid of the mean and median stacked profiles, respectively. The uncertainties in columns 6–9 are estimated from the stacked absorption corresponding to the bootstrap samples. (10) and (11) Column density obtained from the  $W_r$  listed in (6) and (8), respectively, assuming that the line falls in the linear part of the curve of growth.

<sup>a</sup>The velocity range used for single-component Gaussian fitting to the mean absorption profile is  $[-200.0, +500.0]$  km s<sup>-1</sup>.

<sup>b</sup>The velocity range used for single-component Gaussian fitting to the mean absorption profile is  $[-300.0, +300.0]$  km s<sup>-1</sup>.

<sup>c</sup>The velocity range used for single-component Gaussian fitting to the mean absorption profile is  $[-250.0, +500.0]$  km s<sup>-1</sup>.

<sup>d</sup>The velocity range used for single-component Gaussian fitting to the mean absorption profile is  $[-500.0, +200.0]$  km s<sup>-1</sup>.

**Table A2.** Measurements performed on the C IV stacks.

Sample	$V_{\text{offset}}$ (km s <sup>-1</sup> )		$\sigma_v$ (km s <sup>-1</sup> )		$W_r$ (Å)		$W_r$ (Å)		$\log_{10} N(\text{C IV})/\text{cm}^{-2}$	
	Mean	Median	Mean	Median	Mean	Median	Mean	Median	Mean	Median
(1)	(2)	(3)	(4)	(5)	(6)	(7)	(8)	(9)	(10)	(11)
all	-30 ± 22	-18 ± 21	134 ± 23	107 ± 19	0.066 ± 0.017	0.008 ± 0.002	0.070 ± 0.019	0.010 ± 0.003	13.21 ± 0.11	12.39 ± 0.12
all_environment_iso <sup>a</sup>	-31 ± 83	15 ± 31	167 ± 83	107 ± 31	0.062 ± 0.022	0.006 ± 0.002	0.064 ± 0.025	0.007 ± 0.003	13.19 ± 0.16	12.22 ± 0.17
all_environment_group <sup>b</sup>	1 ± 17	-27 ± 23	71 ± 14	69 ± 20	0.070 ± 0.026	0.018 ± 0.010	0.082 ± 0.028	0.020 ± 0.011	13.24 ± 0.16	12.69 ± 0.23
all_ρ_low <sup>c</sup>	-43 ± 18	32 ± 35	69 ± 17	90 ± 43	0.055 ± 0.023	0.009 ± 0.006	0.061 ± 0.025	0.013 ± 0.006	13.13 ± 0.18	12.49 ± 0.22
all_ρ_mid	-105 ± 89	9 ± 25	163 ± 73	55 ± 22	0.048 ± 0.020	0.007 ± 0.005	0.044 ± 0.023	0.008 ± 0.005	13.08 ± 0.18	12.32 ± 0.26
all_ρ_high <sup>d</sup>	-29 ± 31	-43 ± 37	123 ± 29	86 ± 41	0.089 ± 0.042	0.008 ± 0.006	0.094 ± 0.045	0.010 ± 0.006	13.34 ± 0.20	12.39 ± 0.27
iso_ρ_low	-66 ± 22	43 ± 62	77 ± 22	112 ± 62	0.065 ± 0.028	0.010 ± 0.008	0.065 ± 0.030	0.011 ± 0.008	13.21 ± 0.19	12.45 ± 0.32
iso_ρ_mid	89 ± 23	23 ± 36	47 ± 19	38 ± 33	0.022 ± 0.022	0.003 ± 0.004	0.040 ± 0.027	0.005 ± 0.005	12.73 ± 0.43	12.11 ± 0.40
iso_ρ_high	-86 ± 65	-10 ± 23	149 ± 69	44 ± 19	0.074 ± 0.054	0.006 ± 0.005	0.087 ± 0.058	0.005 ± 0.006	13.27 ± 0.31	12.11 ± 0.46
iso_z_peak_low <sup>e</sup>	-22 ± 117	46 ± 34	188 ± 144	83 ± 31	0.067 ± 0.033	0.005 ± 0.003	0.069 ± 0.034	0.006 ± 0.003	13.22 ± 0.22	12.15 ± 0.22
iso_z_peak_high <sup>e</sup>	-29 ± 87	12 ± 51	131 ± 75	105 ± 48	0.061 ± 0.027	0.007 ± 0.005	0.061 ± 0.036	0.009 ± 0.006	13.18 ± 0.19	12.33 ± 0.33
iso_L(Ly α)_low <sup>e</sup>	-131 ± 207	7 ± 36	127 ± 142	70 ± 33	0.041 ± 0.027	0.004 ± 0.004	0.037 ± 0.032	0.005 ± 0.005	13.01 ± 0.28	12.07 ± 0.44
iso_L(Ly α)_high <sup>f</sup>	-11 ± 55	23 ± 57	183 ± 73	94 ± 70	0.082 ± 0.035	0.007 ± 0.004	0.091 ± 0.036	0.008 ± 0.004	13.31 ± 0.18	12.28 ± 0.23
iso_FWHM_low <sup>e</sup>	25 ± 48	25 ± 32	84 ± 45	60 ± 29	0.049 ± 0.024	0.006 ± 0.005	0.064 ± 0.032	0.008 ± 0.006	13.08 ± 0.22	12.28 ± 0.31
iso_FWHM_high	21 ± 61	20 ± 42	174 ± 71	108 ± 42	0.082 ± 0.038	0.006 ± 0.004	0.075 ± 0.038	0.006 ± 0.004	13.31 ± 0.20	12.16 ± 0.29
all_SFR_non-det	-10 ± 29	13 ± 17	87 ± 25	56 ± 15	0.036 ± 0.015	0.007 ± 0.003	0.035 ± 0.017	0.008 ± 0.003	12.96 ± 0.18	12.29 ± 0.17
all_SFR_low	-12 ± 24	-39 ± 53	58 ± 19	85 ± 37	0.049 ± 0.030	0.007 ± 0.006	0.047 ± 0.033	0.007 ± 0.007	13.08 ± 0.27	12.22 ± 0.46
all_SFR_high	85 ± 63	-20 ± 45	82 ± 57	56 ± 42	0.034 ± 0.017	0.005 ± 0.007	0.043 ± 0.029	0.009 ± 0.008	12.92 ± 0.22	12.34 ± 0.39
all_EW0_low	-28 ± 22	-12 ± 24	58 ± 21	45 ± 22	0.043 ± 0.028	0.009 ± 0.009	0.056 ± 0.038	0.012 ± 0.010	13.03 ± 0.28	12.48 ± 0.37
all_EW0_high	82 ± 22	5 ± 60	53 ± 17	101 ± 45	0.030 ± 0.019	0.004 ± 0.003	0.033 ± 0.021	0.005 ± 0.004	12.87 ± 0.27	12.06 ± 0.41

Notes. The same as Table A1 but for C IV. A velocity range  $[-250, +250]$  km s<sup>-1</sup> is used for single-component Gaussian fits, unless specified otherwise.

<sup>a</sup>The velocity range used for single-component Gaussian fitting to the mean absorption profile is  $[-150.0, +250.0]$  km s<sup>-1</sup>.

<sup>b</sup>The velocity range used for single-component Gaussian fitting to the median absorption profile is  $[-150.0, +250.0]$  km s<sup>-1</sup>.

<sup>c</sup>The velocity range used for single-component Gaussian fitting to the median absorption profile is  $[-150.0, +200.0]$  km s<sup>-1</sup>.

<sup>d</sup>The velocity range used for single-component Gaussian fitting to the median absorption profile is  $[-200.0, +200.0]$  km s<sup>-1</sup>.

<sup>e</sup>The velocity range used for single-component Gaussian fitting to the mean absorption profile is  $[-200.0, +250.0]$  km s<sup>-1</sup>.

<sup>f</sup>The velocity range used for single-component Gaussian fitting to the median absorption profile is  $[-150.0, +150.0]$  km s<sup>-1</sup>.

This paper has been typeset from a TeX/L<sup>A</sup>T<sub>E</sub>X file prepared by the author.